

Experimental study on flexural behaviour of prefabricated concrete beams with double-grouted sleeves

Zhiwei Lu^a, Bin Wu^{a,*}, Shaopan Yang^a, Jinyou Hou^a, Zhuangzhuang Ji^a, Yongfu Li^a, Jun Huang^a,
Mingzhong Zhang^b

^a *School of Civil Engineering and Architecture, Wuhan University of Technology, Wuhan 430070, China*

^b *Department of Civil, Environmental and Geomatic Engineering, University College London, London WC1E 6BT, UK*

Abstract: A novel precast concrete beam connected using double-grouted sleeves was developed to reduce pouring concrete on-site and expedite construction. This paper presents a systematic experimental study on the flexural behaviour of precast beams subjected to three-point and four-point bending. In total, 11 specimens with different types of grouted sleeves, diameters of the lower transition bar, filler lengths, numbers of filler, types of filler, types of connection and lengths of the grouted sleeve, and two cast-in-situ specimens were tested. The results indicated that the steel sleeves in the beams performed satisfactorily, and threads aided in increasing their initial stiffness. The first cracking load of all the prefabricated beams was lower than that of the reference beams owing to the interface effect. With an increase in the diameter of the lower transition bar, the yield and ultimate bearing capacities of the precast specimen under three-point bending increased by 9.0% and 21.0%, respectively. The beams with double-grouted sleeves exhibited better ductility with maximum crack widths that were 41.2% and 28.6% larger than that of the reference beam under three-point and four-point bending, respectively. The stress concentration in the filler region occurred owing to discontinuous stiffness but decreased with an increase in the diameter of the lower transition bar. The beam with double steel sleeves achieved a slightly lower normal service load limit than the cast-in-place beam. As the filler length increased by 20 mm, the maximum crack width of the beams with double-grouted sleeves increased by 55.6%. The method for the cast-in-place beam was adequate for calculating the load-bearing capacity of the prefabricated beam with double-grouted sleeves or a single-grouted sleeve.

Keywords: Prefabricated concrete beam; Double-grouted sleeve; Transition rebar; Deflection;

* Corresponding author. E-mail address: wub@whut.edu.cn (B. Wu).

Plastic concentration region

1. Introduction

An increasing number of prefabricated concrete structures have been applied to buildings to replace conventional constructions with cast-in-situ concrete owing to their less manual labour, lower energy consumption, good construction conditions, rapid site installation, and high quality [1-5]. The Chinese government proposed that the ratio of prefabricated structures should be over 30% in new buildings through ten years of effort [6]. Precast concrete structures primarily consist of precast concrete shear walls and frame structures. Prefabricated concrete frame structures are particularly suitable for the building industry because their members are very easy to manufacture, standardise, and erect [7,8]. However, large local deformations and premature damage can occur at the connections between the prefabricated beams and columns in the precast system if not conducted properly, which may result in the rapid failure of the entire structure. This may hinder the widespread use of precast structures in seismic zones. To date, many efforts have been conducted to solve the connection problems. Current beam-column joints can be classified into two general categories: connection in the core zone of the beam-column joint, and connection outside the core region of the beam-column joint.

With respect to the connection in the core zone of the beam-column joint, Alcocer et al. [9] used mild steel rebars and prestressing strands to achieve precast beam continuity and measured two precast concrete beam-column joints. They observed that the structural behaviour of the specimens was satisfactory and suggested that the concentration of precast beam flexural rotations should be kept farther from the precast column faces to improve the cyclic performance of the connections. Parastesh et al. [10] developed a ductile joint for a prefabricated concrete frame and observed that the joints exhibited higher initial stiffness and flexural strength than the control specimens because of the lap splicing of steel bars in the connection region. Guan et al. [11] studied a new type of connection for prefabricated beams with a U-shaped cross-section. They observed that there was no need to develop a short debonded length of the longitudinal rebar in the prefabricated reinforced concrete beams. Ghayeb et al. [12] developed a novel hybrid joint using steel pipes, steel plates, and grouted sleeves to connect precast beams and columns, and they reported that there was less extensive damage to the proposed joint compared with a cast-in-situ specimen. Nevertheless, the connection in the core region of a beam-column joint often results in complicated construction and poor construction quality

of the joint core region with reinforcing bar tying and post-concrete casting [13].

To address these challenges, scholars recently developed a connection outside the core region of the beam-column joint [13-15]. However, although the connection region moved from the beam-column joint core zone, the problems of rebar tying and casting concrete on-site have not been addressed. Welded connections [16,17], dowel pin connections [18-23], bolted connections [24-27], and prestressed connections [28-33] have been proposed and investigated to solve these problems. However, for welded connections, to guarantee the welding quality, particular care (e.g. tolerances should be checked thoroughly) is required when welding the steel rebar, and welding construction is always conducted by experienced workers with special training, which may increase the installation costs [16], while pinned connections are frequently used in low-rise buildings (e.g. single-story industrial buildings) owing to their lower cost and distinctive structural behaviour. Bolted connections may result in extra steel congestion problems and demand very tight tolerances in manufacturing prefabricated concrete components, which may still be a significant challenge for most manufacturers of precast components [34]. For prestressed connections, note that this type of joint using the post-tensioning method frequently requires energy dissipation devices to increase their seismic capacities owing to their lower inherent damping [33]. Additionally, the cost of the prestressed precast beam-column connections may be relatively higher than that of comparable cast-in-place connections [35], and their construction method is also very complex [13].

Thus, a novel method of connecting precast concrete frame structural members has been introduced [42] to overcome the limitations mentioned above for current prefabricated connections (Fig. 1). This method can accelerate on-site installation and aid in saving costs by eliminating casting concrete, tying, bolting, welding, and post-tension steel strands on site. In addition, grouted couplers have the remarkable advantages of large and controllable tolerances, and they have sufficient capacity to splice discontinuous rebars [36-41]. Recently, the mechanical performance of precast beam-column joints with double-grouted sleeves has been experimentally studied [42], whereas the structural behaviour of precast beams with double-grouted sleeves has not been explored.

Several studies have been conducted on the structural behaviour of precast concrete beams because of their importance in ensuring structural safety. For instance, Cleland and Baber [43] explored the performance of precast ledger beams through experimental analysis. They concluded that limiting the length-width ratio and lengths of beams prevented the cracking of finished surfaces

and load eccentricity. Baghdadi et al. [44] experimentally and numerically investigated the flexural behaviour of several precast concrete beams with dry connections and reported that only the beam with a pin and rectangular segment exhibited approximately 85% of the load-bearing capacity of the entire section. Yan et al. [45] explored the impact behaviour of a precast concrete beam with grouted sleeves and observed that the connection location had a significant effect on the impact resistance of the beam and its performance could be similar to that of a monolithic beam when the loading point was farther from the connection location. Le et al. [46] used carbon fibre reinforced polymer (CFRP) tendons to connect prefabricated concrete segmental beams and observed that specimens with CFRP tendons had similar load-deflection responses to the reference beam with steel tendons.

Because the short filler zone between two grouted sleeves is the weak point of the precast beams with double steel sleeves, the three-point bending test method was used in this study to consider the effect of the most unfavourable load. However, compared with the length of the beam, the total length of the short and long grouted sleeves in the beam with double steel couplers is relatively small; therefore, the four-point bending test was also utilised to fully obtain the flexural performance of the precast beam.

This study, for the first time, systematically investigated the flexural behaviour of precast beams connected using double-grouted sleeves through a series of three-point and four-point bending tests. The effects of sleeve type, filler length, filler type, filler number, lower-transition-bar diameter, and loading type on the flexural behaviour of precast beams in terms of load-displacement/strain response, failure mode, displacement ductility, evolution of stiffness, and development of crack width were estimated, and the underlying flexural failure mechanisms of the beams connected using double-grouted sleeves under monotonic loading were explored in depth. In addition, precast beams with single-grouted sleeves and cast-in-place control beams were also prepared and tested for a comprehensive comparison with the precast beams developed in this study.

2. Experimental program

2.1. Test specimens

Thirteen large-scale beams were designed and tested to eliminate the size effect: eleven precast concrete beams and two cast-in-situ concrete beams. All beams had a cross-section of 200 mm × 350 mm and a total length of 4000 mm. The longitudinal steel reinforcement of all beams consisted of two bars with a diameter of 10 mm in the upper part and two bars with a diameter of 16 mm in the

lower part. The transverse steel bar was provided with a rectangular hoop with a diameter of 8 mm and a spacing of 100 mm. Figs. 2 and 3 show the dimensions and steel bar details of the tested specimens.

Two types of grouted sleeves, i.e. grouted sleeve with wedge (GSW) and grouted sleeve with wedge and thread (GSWT), developed and introduced in a recent publication [47], were used in this study. The dimensions of the GSW and GSWT fabricated from steel tubes with a specified yield strength of 390 MPa are shown in Fig. 4 and listed in Table 1. The thickest wall of the wedge was approximately 4 mm, while the thinnest wall of the wedge was approximately 1 mm. The difference between GSW and GSWT is that there are internal threads in the latter, as depicted in Fig. 4b. For labels W-1 and T-1, 'W' and 'T' represent GSW and GSWT, respectively.

The test scenarios were designed to investigate the effects of the diameter of the lower transition bars, length of the filler, number of fillers, filler material, connection type, length of the grouted sleeve, and type of grouted sleeve. Two diameters of 16 and 18 mm were selected for the lower transition bars, 35 and 55 mm for the filler length, one or two for the filler numbers in a precast specimen, high-strength grouting mortar and common grouting concrete for the filler material, single- and double-grouted sleeves for the connection type, and 280 and 400 mm for the sleeve length in the connections with single-grouted sleeves. Two scenarios of loading were considered to study the influences of pure bending and coupled bending and shear on the behaviour of the fillers. The specimen design details are summarised in Table 2.

2.2. Materials

The average compressive strengths of precast and post-cast concrete were obtained from a test on concrete cubes with dimensions of 150 mm × 150 mm × 150 mm. According to JG/T408 [48], prism specimens with dimensions of 40 mm × 40 mm × 160 mm were used to measure the compressive and flexural strengths of the grout and filler. The mechanical properties of precast concrete, post-cast concrete, grout, grouting mortar, and reinforcement (HRB 400) obtained from uniaxial compressive and tensile tests are presented in Tables 3 and 4.

2.3. Specimen preparation

Fig. 5 shows the manufacturing process of the tested prefabricated specimens, which included following steps: (a) The reinforcement cages with steel couplers for precast beams connected using double-grouted sleeves (Fig. 5a1) or without steel couplers for precast beams connected using single-

grouted sleeves (Fig. 5a2) were placed in the wooden formwork; (b) the concrete of all precast members and cast-in-place specimens was cast into the wooden formwork; (c) the precast members were separated for installation; (d) the surface of prefabricated beam end was intentionally roughened; (e) the transition bars were prepared; (f) four transition bars were installed into the corresponding steel couplers; (g) the precast concrete component was moved to the designed location, and the transition bars were adjusted to the designed location; (h) the formwork for casting filler was constructed; (i) the grout was prepared for grouting steel sleeves; (j) the steel sleeves were grouted using a pressure machine; (k) the filler (i.e. grouting mortar or post-cast concrete) for the beams with double-grouted sleeves was poured into the formwork; (l) the post-cast concrete was cast for the beams connected by single sleeve; (m) all the specimens were cured for more than 28 days and one face of each was whitewashed and drawn with the grid of $100\text{ mm} \times 70\text{ mm}$ to observe cracks conveniently.

Note that steps (f) and (g) for the precast specimens with double-grouted sleeves were different from the standard installation approach using nipper pliers because the strain gauge was attached to the surface of the transition bars. Thus, the transition bars could not be placed into long steel sleeves before installation. More details on the standard installation approach of precast concrete components connected using double-grouted steel couplers are available in [42].

2.4. Test setup and loading

Figs. 6 and 7 show the loading details and instrumentation of the specimens under three-point and four-point bending configurations with a pure bending zone of 915 mm, respectively. All specimens were simply supported and tested using a clear span of 3600 mm according to GB/T 50152-2012 [49]. Displacement gauges and strain gauges were applied to acquire the beam deflection and strain of the reinforcing bars and steel couplers, respectively. The crack widths at some crucial regions in the specimens were observed using a handheld microscope (Fig. 6b). A hydraulic actuator with a maximum capacity of 500 kN was used to exert a vertical load. The dimensions of the loading plate were $100\text{ mm} \times 250\text{ mm} \times 20\text{ mm}$, and those of the upper plate of the knife edge support (i.e. pin support) and roller support were $200\text{ mm} \times 200\text{ mm} \times 30\text{ mm}$ and $200\text{ mm} \times 200\text{ mm} \times 35\text{ mm}$, respectively. The heights of the two supports were both 110 mm, including the upper plates, lower plates, and knife edge or roller rod. Hybrid loading schemes for load and displacement were conducted in this study. A slow loading process was selected to facilitate the observation of crack

evolution. Because the stiffness of the beams was larger before yielding, a load-control loading protocol with a loading rate of 2 kN/min was selected. After the yielding of the beams, their stiffness became very small; thus, the displacement-control loading protocol was applied with a displacement rate of 3 mm/min. During the tests, the load, displacement, and strain data were acquired and recorded simultaneously using data acquisition systems, and the sampling rate was 2 Hz.

3. Results and discussion

3.1. Bending and shear behaviour of beams

3.1.1. Load-displacement response

Fig. 8a shows the load-displacement response at the midspan for all four specimens under three-point bending. As shown in Fig. 8a, the shapes of the curves of the precast and control specimens were basically the same and contained three inflexion points: cracking, yield, and peak points. Thus, the load-deflection response can be divided into four stages (Fig. 8b). Because the load data at the first turning points, i.e. the cracking points, caused by the major cracks shown in Fig. 8, were higher than those causing early cracks, the load value at the first inflexion point in the load–displacement curves was defined as the major cracking load. As the load increased, the second turning point occurred because of the yielding of the tensile reinforcement. Thereafter, the load values did not change significantly, whereas the deflections increased rapidly. Finally, the beams failed as a result of concrete crushing in the compressive region, which resulted in a decrease in the load-deflection curves.

The feature parameters of the loads and midspan deflections, including the yield, peak, and failure points, are summarised in Table 5. The yield loads of specimens TP-1 and TP-3 were 5.8% larger and 2.4% smaller than that of specimen TC-C, respectively, which revealed that the yield load of the precast specimens was approximate to that of the cast-in-place control specimen. The yield load value of specimen TP-2 was 9% greater than that of specimen TP-1, suggesting that increasing the lower transition bar diameter effectively enhanced the yield load of the precast beam. The peak loads of specimens TP-1 and TP-3 were 6.2% and 7.9% greater than that of specimen TC-C, respectively. This indicated that the presence of grouted couplers and high-strength grouting mortar slightly increased the load capacity of the precast beams, and the strength of the double-grouted sleeve joint was sufficient and greater than that of the cast-in-place beam. However, the improvement was limited and related to the type of loading on the beam because the steel sleeves and the high-strength grouting

filler only existed in the local area of the beam. The peak load value of specimen TP-2 was 21.0% larger than that of specimen TP-1. Fig. 9 shows a comparison of the bending moments of the beams with various tensile-transition-bar diameters. The bending moments of cross-sections D-D and C-C for the beam with a transition-rebar diameter of 16 mm were M_1 and M_3 , respectively. As the diameter of the transition rebar increased by 2 mm, the resistance of cross-section D-D significantly increased, and cross-section C-C became the load-bearing capacity control section of the beam. Note that the resistance of cross-section D-D of specimen TP-2 was significant owing to the smaller tensile crack width at cross-section D-D in specimen TP-2 compared with specimen TP-1 (Figs. 10b and c). Hence, when bending moment M_3 increased to M_1 (i.e. $M'_3 = M_1$), the midspan cross-section bending moment of M_2 increased to M'_2 . Therefore, as expected, an enhancing effect on the local flexural capacity in the area of the filler was achieved by increasing the bearing capacity of the transition rebar. Specimen TP-3 achieved only a 1.7% higher peak load value than specimen TP-1, which suggested that increasing the number of grouted couplers had a minor impact on the flexural capacity of the beam under three-point loading.

3.1.2. Cracking and failure modes

Fig. 10 shows the final observation of the beams under three-point bending. Generally, all beams exhibited flexural cracks during the initial loading phase, and with further loading, some of the flexural cracks turned into flexural-shear cracks and eventually shear cracks. However, the opening of the interfaces with long and wide straight cracks in all precast beams was observed, and the crack distribution of precast specimens TP-1, TP-2, and TP-3 was significantly different from that of the cast-in-situ specimen TC-C. The wide cracks for the cast-in-place beam TC-C appeared on the tension face near the loading point, while the wide cracks in beam TP-1 were located at the interfaces between the precast concrete and filler, which can be attributed to the higher strength of the grouted couplers on both sides of the filler compared with steel bars. As the load increased, the transition bars on the tension side of beam TP-1 exhibited a larger axial elongation deformation than the steel couplers, which resulted in wide cracks at the interfaces between the filler and precast concrete. However, for specimen TP-2, with the increased diameter of the lower transition bar, the widths of the cracks at the interfaces between the filler and precast concrete decreased significantly. The wide cracks formed at the left end of the short steel sleeves and the right end of the long steel sleeves. Unlike other precast beams, specimen TP-3 with a single grouted sleeve had approximately five wide cracks, which were

more than those of specimens TP-1 and TP-2 with only two wide cracks. This was because only one grouted sleeve with a short length on a single longitudinal bar was located in the midspan of specimen TP-3. As a result, the crack suppression range of the grouted sleeve in beam TP-3 was smaller than those of beams TP-1 and TP-2. As shown in Table 6, the first cracking load of the precast beam with double-grouted or single-grouted sleeves was 66.7% smaller than that of the reference beam as a result of the influence of the interface between the precast concrete and filler.

3.1.3. Displacement ductility

The displacement ductility ratio is an important parameter for evaluating the ductility of inelastic components, and it is defined as the coefficient of the failure midspan deflection (Δ_F) to the midspan deflection (Δ_Y) when the beam yields:

$$\mu_{\Delta} = \frac{\Delta_F}{\Delta_Y} \quad (1)$$

Note that the failure point was originally intended to be defined as that on the load-midspan deflection curve when the load decreased by 15% of the peak value. However, the first tested specimen FP-2, presented in Section 3.2, fractured abruptly and destroyed the displacement gauges attached to the bottom of the specimen. Therefore, the loading was stopped when the recorded load decreased after its peak value for the specimens after FP-2. Consequently, the last recorded data of the load and displacement were defined as the failure point. The displacement ductility ratios for the beams under three-point bending are listed in Table 5. The larger the ductility, the safer the structure was. The ductility coefficients of specimens TP-1 and TP-3 were 24.4% and 31.8% larger than that of the control specimen TC-C, respectively, which implied that the beams with double-grouted couplers or single-grouted sleeves had excellent ductility behaviour. The ratio μ_{Δ} of specimen TP-2 was 3.4% greater than that of specimen TP-1, which revealed that increasing the tensile transition bar diameter had a minor effect on the ductility of the precast beam connected using double steel couplers. In addition, μ_{Δ} of specimen TP-1 was 6.0% smaller than that of the specimen TP-3, which suggested that decreasing the number of grouted couplers could slightly increase the ductility of the beam.

3.1.4. Evolution of stiffness

The stiffness degradation under loading can represent the accumulation of internal structural damage and the structural capacity to resist deformation, which can be used to evaluate the mechanical behaviour of a structural member and aid in the design and modelling of a structural subassembly

[50-54]. The initial stiffness K_1 , secondary stiffness K_2 , and third equivalent stiffness K_3 can be calculated based on the characteristic parameters obtained from Tables 5 and 6, which can be described as follows:

$$K_1 = \frac{F_T}{\Delta_T}; K_2 = \frac{F_Y - F_T}{\Delta_Y - \Delta_T}; K_3 = \frac{F_P - F_Y}{\Delta_P - \Delta_Y} \quad (2)$$

The stiffness degradation of the specimens under three-point bending is shown in Fig. 11. K_1 of the control specimen TC-C was 12.47 kN/mm, which was 12.9%, 41.2%, and 21.1% higher than that of specimens TP-1, TP-2 and TP-3, respectively. This distinctive difference can be attributed to the very small or negligible tensile strength of the interfaces between the precast and post-cast concrete or grouting mortar because of the discontinuity of concrete and the initial small slip between the grout and the inner wall of the sleeve; thus, the interfaces were prone to cracking and the cracking loads at the interfaces of the precast beams were not more than 2 kN (Table 6). Note that during installation, the specimen TP-2 was subjected to slight impact loads. Accidental loading caused one fine crack at the left flexural-shear zone, five fine hairline cracks at the right flexural-shear region, and one fine hairline crack at the interface between the filler and prefabricated concrete. Therefore, K_1 of specimen TP-1 was 25.1% greater than that of specimen TP-2. Moreover, K_1 of beam TP-1 was higher than that of beam TP-3 because increasing the number of grouted sleeves in a single longitudinal bar increased the length of the local concrete reinforced with grouted sleeves with large stiffness, which increased the global stiffness of the specimen. When the number and extension of cracks reached a certain degree, the stiffness of the beam began to decline, and the first turning point on the load-displacement curves appeared.

As shown in Fig. 11, K_2 of control beam TC-C was similar to that of precast beams TP-1 and TP-3. However, K_2 of beam TP-2 was 4.63 kN/mm, which was 18.7% greater than that of beam TP-1, which indicated that increasing the lower transition bar diameter could significantly increase the secondary stiffness of the precast beam with double-grouted couplers. This was because the enhancement of the tension capacity of the lower transition bar on the tension face of the beam decreased the rotation capacity and deformation of the beam before the yielding of the beam. When the specimens yielded, the stiffness decreased significantly, and the K_3 values of all the specimens were very approximate to each other.

3.1.5. Load-strain response

Fig. 12 shows the load-strain response of the steel bars in the beams under three-point bending. As shown in Figs. 12a and b, the evolution of the strain of the tensile and compressive transition rebar against load in beam TP-1 was different from that of tensile and compressive longitudinal rebar in the midspan section of beam TC-C. The strain of strain gauge #16 exhibited an almost linear response before yielding, but after the lower transition rebar and beam almost simultaneously yielded, the strain decreased steeply and subsequently increased unsteadily. This can be attributed to the interface that was easy to crack at a lower load, resulting in the lower transition rebar bearing the tension force prematurely and alone when the interface cracked. In addition, the strain changed abnormally after the beam yielded, which may have been caused by the non-uniform shrinkage of the lower transition rebar with a shorter length in the filled local region, resulting in an abnormal operation of the strain gauge. This phenomenon was also observed in other specimens. The load-strain responses for strain gauges #12, #19, and #20 in specimen TP-1 were similar to those for strain gauges #11, #15, and #16 in specimen TC-C. The maximum average compressive strain of strain gauges #5 and #6 in beam TP-1 was significantly greater than that of strain gauges #3 and #4 in beam TC-C, respectively, which indicated the presence of stress concentration in the filler region. This was due to the rotation being concentrated in the filled area for beam TP-1 because the region reinforced with steel sleeves with large stiffness only underwent rigid body rotation compared with the cast-in-situ beam TC-C (Fig. 13). For similar reasons, stress concentrations also existed at the left end of the short steel sleeve and the right end of the long steel sleeve in beam TP-1 (Figs. 12a and b).

As shown in Fig. 12c, the yielding of beam TP-2 was controlled by the yielding of the lower longitudinal rebar at the left end of the short steel couplers and the right end of the long steel couplers owing to the increase in the lower transition rebar diameter, which was different from that of beam TP-1. All measuring points in the compression zone tended to be under tensile strain, and some of them eventually underwent tensile strain after the yielding of beam TP-2, which may have been caused by the tension crack passing through the upper reinforcement of the beam. As shown in Figs. 12b and c, increasing the diameter of the tensile transition rebar decreased the strain of the compressive transition rebar and stress concentration in the joint area. However, the stress concentration problem has not yet been completely resolved. Thus, the diameter, strength, diameter, and strength of the compressive transition rebar should be increased to further cope with the stress concentration. Similar findings were also observed in the specimens subjected to four-point bending.

Note that the maximum strain of the strain gauges on the steel couplers in all the prefabricated beams was lower than the yield strain of $1893 \mu\epsilon$, which suggested that the strength of the sleeves used in this study was sufficient.

3.1.6. Development of crack width

Fig. 14 shows the load-crack width curves for selected cracks in the specimens under three-point bending. The maximum crack width of beams TC-C and TP-3 was 3.5 mm, which was 41.2% and 58.3% lower than those of specimens TP-1 and TP-2, respectively. The same maximum crack width of the beam with a single-grouted sleeve as that of the control beam can be attributed to the crack distribution in specimen TP-3 in terms of the number and crack width being very close to that of the control specimen owing to the lower length of the steel couplers (Figs. 10a and d). However, as the number of steel sleeves increased, the maximum width of the beam was significantly increased owing to the larger stiffness and strength in the zones reinforced by steel couplers, which resulted in concentrated failure at the end of the steel sleeve. In addition, as the diameter of the lower transition bar increased, the location of the maximum crack shifted from one end of the steel sleeve to the other, and the maximum crack width decreased by 29.4% (Figs. 14b and c). Note that the crack width in the region of the steel couplers (e.g. CK2 and CK3 for beam TP-1) increased linearly throughout and was significantly smaller than other cracks because of the influence of steel couplers with higher strength.

Cracks affect the appearance of buildings, and wide cracks cause reinforcing bars to corrode. Therefore, the crack width should be limited to a certain range. According to GB50010-2010 [55], the maximum crack width limit of reinforced concrete structures is 0.2 mm. Herein, the normal service load limits of the beams were compared using the load-bearing capacity corresponding to a crack width of 0.2 mm, which can be considered to be the serviceability limit state for this study (Fig. 14e). The load value of beam TP-1 was 29.8% lower than that of reference beam TC-C. Nevertheless, as the lower transition bar diameter was increased by 2 mm, the load value of the beam with double-grouted couplers increased by 32.9%, which was only 6.7% smaller than that of the reference beam. This implied that increasing the tensile capacity of the lower transition bars for the beam with double-grouted couplers can significantly improve the normal service load limit under the serviceability limit state and aid the beam with double steel sleeves in achieving a normal service load limit only slightly lower than that of the cast-in-place beam. Moreover, the load value of beam TP-3 was 15.8% greater and 12.9% lower than that of beams TP-1 and TP-2, respectively. This suggested that by increasing

the diameter of the lower transition steel bars, the normal service load limit of the beam with double steel sleeves can be greater than that of the beam with a single grouted sleeve under the serviceability limit state.

3.2. Pure bending behaviour of beams

3.2.1. Load-displacement response

Fig. 15 shows the load-displacement response at the midspan for the tested specimens under four-point bending. The feature parameters of the loads and midspan deflections of the specimens are listed in Table 5. The yield loads of specimens FP-1, FP-2, FP-3, FP-4, FP-5, FP-6, FP-7, and FP-8 were 5.1%, 0.9%, 5.0%, 1.3%, 4.3%, 4.4%, 10.9%, and 9.9% lower than those of the reference specimen FC-C, respectively, indicating that all the precast beams under pure bending had a lower yield load than the cast-in-place beam.

As shown in Table 5, the peak loads of beams FP-1 and FP-6 were 4.3% and 4.1% smaller than those of the reference beam FC-C, respectively. This indicated that the load-carrying capacity of the precast beam with double-grouted sleeves under four-point bending was similar to that of the cast-in-place specimen, which was different from that of the precast specimens subjected to three-point bending. This was because the loading point of the precast specimens under four-point bending was farther from the steel sleeves, which resulted in the bearing capacity of the beam being determined by the load capacity of the steel bar and the strength of the concrete or filler at the end of the steel sleeve. The maximum load capacity of specimen FP-2 was only 1.8% higher than that of specimen FP-1, indicating that the threads in the steel sleeve had a minor effect on the bearing capacity of the precast beam, and the grouted sleeve without built-in threads performed satisfactorily in this new connection. The bearing capacity of specimen FP-3 was only 2.4% higher than that of FP-1. This was because the lower transition bar with a larger tensile load capacity only increased the resistance force of the filler area, and the tensile capacity of the lower longitudinal bars located in the zones below the two loading points did not change. Thus, increasing the load capacity of the tension transition bar did not significantly enhance the maximum load capacity of the precast beam. The load-bearing capacity of beam FP-4 was 2.0% greater than that of beam FP-1, which indicated that increasing the length of the filler did not increase the bearing capacity of the beam. The maximum load value of beam FP-5 was 0.2% higher than that of beam FP-4, which indicated that the use of ordinary concrete instead of high-strength grouting mortar almost did not affect the bearing capacity. The maximum

load-carrying capacities of specimens FP-7 and FP-8 were 1.9% larger and 2.5% smaller than those of specimen FP-1, respectively. This suggested that the beam with double-grouted couplers under four-point bending had a similar flexural load capacity as the beam with a single-grouted sleeve.

3.2.2. Cracking and failure modes

Although the crack distributions of precast specimens FP-1, FP-2, FP-3, FP-4, FP-5, FP-7, and FP-8 were significantly different from those of the cast-in-place beam FC-C, all the specimens including the precast and cast-in-situ specimens exhibited flexural failure, and the distribution range of their wide cracks was basically the same (Fig. 16). The wide cracks of specimens FC-C and FP-6 were evenly distributed in the middle span of approximately 1300 mm. However, the wide cracks in specimens FP-1, FP-2, FP-4, and FP-5 were primarily distributed in the two areas, i.e. the area below the two loading points and the filler area. In addition, the wide cracks of specimens FP-3, FP-7, and FP-8 were only distributed in the two areas below the two loading points. Therefore, we observed that specimens FC-C and FP-6 only had a long plastic concentration area, while specimens FP-1, FP-2, FP-4, and FP-5 and specimens FP-3, FP-7, and FP-8 had three and two short plastic concentration areas, respectively. This was because the steel couplers increased the local stiffness and strength of the beam, which resulted in the failure and larger rotation occurring only at the two ends of the grouted steel couplers. In addition, the embedded grouted sleeves of specimen FP-6 were farther from the loading points, and their stiffness and strength in the middle span of more than 1300 mm were continuous. Consequently, the crack pattern and plastic concentration areas of specimen FP-6 were very similar to those of the cast-in-situ specimen FC-C. In comparison with specimen FP-1, specimen FP-3 with double-grouted sleeves only had two plastic concentration areas, and its failure mode was very similar to that of specimens FP-7 and FP-8 with a single grouted sleeve. This can be attributed to the increased diameter of the lower transition bar, which decreased the rotation capacity of the filler zone. Thus, the number of wide cracks in FP-3 was less than that of the other specimens. Similar to the beams under three-point bending, the average first cracking loads of the precast beams with double-grouted sleeves under four-point bending were 55.2% lower than those of the reference beam (Table 6). The average first cracking load of the prefabricated beam with a single grouted sleeve under four-point bending was 87.5% lower than that of the reference beam. All the first cracks occurred at the interface between the precast concrete and filler. This may result in premature corrosion of the reinforcing bars in the beam. In addition, the interfaces deemed as weak points can easily produce

wide cracks because of discontinuous concrete [56]. Note that for the proposed beams connected by double-grouted sleeves, this problem can be effectively solved by replacing the transition rebar with a fibre-reinforced polymer rebar.

3.2.3. Displacement ductility

The displacement ductility ratios μ_{Δ} of the beams under four-point bending are presented in Table 5. The ductility ratios for specimens FP-1 to FP-8 were 7.0% to 41.1% higher than those of the reference specimen FC-C, which further suggested that the ductility of the prefabricated beam with double-grouted or single-grouted sleeves was better than that of the cast-in-situ beam. This can be explained by the larger crack width located in the grouted sleeve end resulting in a larger rotation of the beam compared with the cast-in-place beam. μ_{Δ} of specimen FP-2 was 24.2% greater than that of specimen FP-1, which was a result of the larger failure displacement of specimen FP-2 compared with specimen FP-1. μ_{Δ} of specimen FP-3 was 3.1% lower than that of specimen FP-1, which implied that increasing the lower transition bar diameter had a minor effect on the ductility of the prefabricated beam under four-point bending. However, increasing the gap length improved the ductility of the prefabricated beam, and the filler with higher strength grouting mortar than common concrete could provide better ductility because the μ_{Δ} of specimens FP-4 and FP-5 was 12.3% and 4.0% higher than that of specimen FP-1, respectively. This was because the increased elongation capacity of the bottom transition reinforcement caused by the increased connecting gap length increased the rotation capacity of the infill zone. In addition, moving the connection position of the prefabricated beam from the midspan area to both ends slightly improved the ductility because the ductility ratio of specimen FP-6 was 6.1% greater than that of specimen FP-1. Additionally, the ductility coefficients of specimens FP-7 and FP-8 were 27.8% and 11.8% larger than that of specimen FP-1, respectively. This indicated that the ductility of a beam with double-grouted sleeves under four-point bending is lower than that of a beam with a single sleeve, and increasing the length of the steel sleeve in the beam with a single sleeve may decrease its ductility.

3.2.4. Evolution of stiffness

The stiffness degradations of the specimens under four-point bending are shown in Fig. 17. K_1 of the control specimen FC-C was 21.8 kN/mm, which was 22.2% to 89.7% larger than that of the specimens FP-1, FP-3, FP-4, FP-5, FP-6, FP-7 and FP-8. This indicated that K_1 of the precast beams was significantly lower than that of the monolithic beam. This result was consistent with the previous

experimental results of the specimens under three-point bending, and the corresponding discussion is presented in Section 3.1.4. However, K_1 of the beam with double-grouted sleeves could be improved by increasing the bond strength between the grouted material and the inner wall of the sleeve through the internal threads in the sleeve, which was supported by the observation that specimen FP-2 developed a 134% larger initial stiffness than specimen FP-1 (Fig. 17a). Compared with specimen FP-1, K_1 of specimen FP-3 with a larger lower transition bar did not change significantly (Fig. 17b). As shown in Fig. 17c, increasing the length of the filler can aid in enhancing the initial stiffness. As shown in Fig. 17d, keeping the assembly location away from the loading point could increase the initial stiffness of the precast beam. In addition, Fig. 17e shows that the initial stiffness of the specimen with a single sleeve was smaller than that of the specimen with double-grouted sleeves, which was the same as the results of the beam under three-point bending. In addition, K_2 and K_3 of the control beam FC-C were similar to those of all the precast beams.

3.2.5. Development of crack width

Fig. 18 depicts the development of the width for selected cracks in the beams under four-point bending with increasing load. The maximum crack width of beam FC-C was the same as that of beam TC-C, indicating that the loading condition of one-point and two-point loading had no influence on the maximum crack width of the cast-in-place beam. However, the maximum crack width of beam FP-7 was 57.0% larger than that of beam TP-3, and the maximum crack widths of beams FP-1 and FP-3 were 47.1% and 33.3% smaller than those of specimens TP-1 and TP-2, respectively. This indicated that the loading condition has a significant influence on the maximum crack width of prefabricated beams. The maximum crack width of beam FP-1 was 28.6% larger than that of the reference beam FC-C owing to the stress concentration resulting from the discontinuous distribution of the stiffness caused by the double-grouted sleeves. Note that because beam FP-2 was continuously loaded to the fractured state, the measured maximum crack width was significantly greater than that of beam FP-1. As the gap between the precast parts increased from 35 to 55 mm for specimens FP-1 and FP-4, the maximum crack width increased by 55.6% (Figs. 18b and e). This can be attributed to the increased longitudinal elongation capacity of the lower transition bars in the gap region with increasing length. As shown in Figs. 18a and g, the overall behaviour of the load-width response of specimen FP-6 was very similar to that of beam FC-C, and the maximum crack width of the interfaces at the two ends of specimen FP-6 was very small owing to the lower flexural moment and shear force.

In addition, the maximum crack width of specimen FP-8 decreased by 9.1% with an increase in the length of the steel couplers from 280 to 400 mm compared with specimen FP-7.

Fig. 18j depicts a comparison of the normal service-load limits. Similar to the beams under three-point bending, the normal service load limits of both the beam with double-grouted sleeves and the beam with a single sleeve under four-point bending were lower than that of the control beam. Although increasing the diameter of the transition steel rebar did not significantly enhance the normal service load limit under the serviceability limit state because two-point loading did not place the beam in the most unfavourable state, the beam with double steel sleeves achieved a normal service load limit that was only slightly lower than that of the cast-in-place beam. In addition, compared with the beam under three-point bending, the normal service load limit of the beam with double steel sleeves subjected to four-point bending under the serviceability limit state was also better than that of the beam with a single grouted sleeve because beam FP-3 achieved a 5.5% greater normal service load limit than beam FP-8.

3.3. Comparison with GB50010-2010

In this section, the load-carrying capacity of the tested beams is predicted and compared with the measured data. Since no bond-slip failure occurred in the connections in the prefabricated beams and the experimental flexural capacity of the prefabricated beams was close to that of the cast-in-place beams, the calculation approach for cast-in-place specimens was used to predict the flexural capacity of the prefabricated beams with double- or single-grouted sleeve splices with the following simplifying assumptions and considerations [55]: (1) the cross-section of the beam remains plane throughout the bending process; (2) the tensile strength of concrete or filler can be ignored owing to its low strength compared with tensile steel bars; (3) the lower strength between filler and precast concrete is selected as the compression strength of beams TP-1, TP-2, FP-1, FP-2, FP-4, and FP-5 for calculation, because the control cross-section of ultimate load capacity of these beams is in the connecting zone; (4) the effects of the grouted steel sleeves in the compression zone are ignored on the stress distribution of concrete or filler.

Fig. 19 shows a schematic for calculating the load-carrying capacity of the beam. According to the classical flexural strength calculation method [55], the following equation can be obtained:

$$\alpha_1 f_c b x = f_s A_s - f'_s A'_s \quad (3)$$

where α_1 is the coefficient of the equivalent rectangular stress, and it is set as 1.0 according to the

specification of GB50010-2010 [55]; f_c is the axial compressive strength of the concrete and is equal to $0.88\alpha_{c1}\alpha_{c2}f_{cu}$ with $\alpha_{c1} = 0.76$, $\alpha_{c2} = 1$, and f_{cu} being the cubic compressive strength of the concrete in the light of [55]; b is the cross-section width of the beam; f_s and f'_s are the tension and compression strengths of the reinforcement, respectively; A_s and A'_s represent the areas of tensile and compressive reinforcement, respectively; x is the compressive height. If x is less than $2a'_s$, which held for all the beams in this study, the ultimate bending strength can be expressed as

$$M_{pre} = f_s A_s (h_0 - a'_s) \quad (4)$$

Subsequently, the flexural capacity (F_{pre}) of the beams can be obtained as

$$F_{pre} = 2 \frac{M_{pre}}{l_\Delta} \quad (5)$$

where l_Δ is the distance from the left support of the beam to its control cross-section for the ultimate load capacity, which is listed in Table 7. The predicted ultimate load-bearing capacities of the specimens are listed in Table 7. The average values of F_{pre}/F_{exp} for the beams with double-grouted steel sleeves and the beams with single steel sleeves were 1.03 and 1.11, which were very close to the value of 1.09 for the reference beams. This indicated that the ultimate strength of prefabricated beams can be adequately predicted as a cast-in-situ beam. In addition, as shown in Table 7, the average value and standard deviation of F_{pre}/F_{exp} for all the tested beams were 1.06 and 0.049, respectively. Such good agreement between the predictions and experimental results further confirmed that the ultimate load-bearing capacity of all the tested beams can be accurately predicted using the classical approach. In addition, the cross-section should be selected carefully and correctly when checking the bearing capacity of the beam with double-grouted steel sleeves.

4. Conclusions

This paper presents a systematic experimental study on the flexural behaviour of a new type of prefabricated beam connected using double-grouted couplers under three-point and four-point bending. Based on the experimental results and theoretical predictions, the following conclusions can be drawn:

- Stress concentration was observed in the filler region owing to the discontinuity of the concrete and stiffness in the precast beam. The average first cracking loads of the prefabricated beams under three-point and four-point bending were observed to be 66.7% and 55.2% lower than those of the corresponding cast-in-situ reference beams, respectively. All the first cracks in the

prefabricated beams occurred at the interface between the prefabricated concrete and the filler.

- The precast beams connected using double-grouted sleeves exhibited a load-bearing capacity similar to the monolithic beams because the grouted sleeves were located only in the local area of the precast beam. The method for predicting the load-carrying capacity of the cast-in-place beam was applied to the precast beams developed in this study.
- With an increase in the lower transition bar diameter, the yield and peak loads of the precast specimen under three-point bending increased by 9.0% and 21.0%, respectively. This was because the lower transition reinforcement was located in the control section of the beam. However, the increase in the lower transition bar diameter had no influence on the yield and ultimate bearing capacities of the precast specimen under four-point bending, which can be attributed to the section controlling the bearing capacity not being in the filler zone.
- The displacement ductility ratio of the prefabricated beam with double-grouted sleeves under three-point and four-point bending was 24.4% and 10.4% greater than that of the control beam, respectively. This indicated that the beam with double-grouted sleeves had a better performance than the cast-in-place beam in terms of ductility.
- The maximum crack widths of the beams with double-grouted sleeves under three-point bending and four-point bending were 41.2% and 28.6% greater than that of the corresponding casting-in-place beams, respectively, which can be attributed to the stress concentration at the end of the steel sleeves in the precast beam. As the gap between the prefabricated parts increased from 35 to 55 mm for the specimens with double-grouted sleeves, the maximum crack width increased by 55.6%. This can be attributed to the increased longitudinal elongation capacity of the lower transition bars in the gap region with an increase in their length.

Acknowledgments

The authors gratefully acknowledge the financial support from the National Key Research and Development Program of China (Grant No. 2016YFC0701106) and the Scientific and Technological Plan Project of Wuhan Urban and Rural Construction Commission (Grant Nos. 202023 and 201910).

M. Zhang gratefully acknowledges the financial support from the Engineering and Physical Sciences Research Council (EPSRC), UK, under Grant Nos. EP/R041504/1 and 1836739, as well as the Royal Society, UK, under Award No. IEC\NSFC\191417.

References

- [1] Priestley MJN. Overview of PRESSS research program. *PCI Journal* 1991;36(4):50-57.
- [2] Kurama YC, Sritharan S, Fleischman RB, Restrepo JL, Henry RS, Cleland NM, et al. Seismic-resistant precast concrete structures: State of the art. *Journal of Structural Engineering* 2018;144:031180014.
- [3] Fan JJ, Feng DC, Wu G, Hou ST, Lu Y. Experimental study of prefabricated RC column-foundation assemblies with two different connection methods and using large-diameter reinforcing bars. *Engineering Structures* 2020;205:110075.
- [4] Ghayeb HH, Razak HA, Ramli Sulong NH. Performance of dowel beam-to-column connections for precast concrete systems under seismic loads: A review. *Construction and Building Materials* 2020;237:117582.
- [5] Lu C, Dong BQ, Pan JL, Shan QF, Hanif A, Yin Wanyun. An investigation on the behavior of a new connection for precast structures under reverse cyclic loading. *Engineering Structures* 2018;169:131-140.
- [6] Wu G, Feng DC. Research progress on fundamental performance of precast concrete frame beam-to-column connections. *Journal of Building Structures* 2018;39(2):1-16.
- [7] Feng DC, Wu G, Lu Y. Finite element modelling approach for precast reinforced concrete beam-to-column connections under cyclic loading. *Engineering Structures* 2018;174: 49-66.
- [8] Guan DZ, Jiang C, Guo ZX, Ge HB. Development and seismic behavior of precast concrete beam-to-column connections. *Journal of Earthquake Engineering* 2016;22(2):234-256.
- [9] Alcocer SM, Carranza R, Perez-Navarrete D, Martinez R. Seismic tests of beam-to-column connections in a precast concrete frame. *PCI Journal* 2002;47(3):70-89.
- [10] Parastesh H, Hajirasouliha I, Ramezani R. A new ductile moment-resisting connection for precast concrete frames in seismic regions: An experimental investigation. *Engineering Structures* 2014;70:144-157.
- [11] Guan DZ, Guo ZX, Xiao QD, Zheng YF. Experimental study of a new beam-to-column connection for precast concrete frames under reversal cyclic loading. *Advances in Structural Engineering* 2016;19(3):529-545.
- [12] Ghayeb HH, Abdul Razak H, Ramli Sulong NH. Seismic performance of innovative hybrid precast reinforced concrete beam-to-column connections. *Engineering Structures* 2020;202:109886.

- [13] Yan QS, Chen TY, Xie ZY. Seismic experimental study on a precast concrete beam-column connection with grout sleeves. *Engineering Structures* 2018;155:330-344.
- [14] Ma CL, Jiang HB, Wang ZY. Experimental investigation of precast RC interior beam-column-slab joints with grouted spiral-confined lap connection. *Engineering Structures* 2019;196:109317.
- [15] Maya LF, Zanuy C, Albajar L, Lopez C, Portabella J. Experimental assessment of connections for precast concrete frames using ultra high performance fibre reinforced concrete. *Construction and Building Materials* 2013;48:173-186.
- [16] Korkmaz HH, Tankut T. Performance of a precast concrete beam-to-beam connection subject to reversed cyclic loading. *Engineering Structures* 2005;27(9):1392-1407.
- [17] Ersoy U, Tankut T. Precast concrete members with welded plate connections under reversed cyclic loading. *PCI Journal* 1993;38(4):94-100.
- [18] Lacerda MMS, Da Silva TJ, Alva GMS, Lima MCV. Influence of the vertical grouting in the interface between corbel and beam in beam-to-column connections of precast concrete structures - An experimental analysis. *Engineering Structures*. 2018;172:201-213.
- [19] Mezzapelle PA, Scalbi A, Clementi F, Lenci S. The influence of dowel-pin connections on the seismic fragility assessment of RC precast industrial buildings. *The Open Civil Engineering Journal* 2017;11:1138-1157.
- [20] Clementi F, Scalbi A, Lenci S. Seismic performance of precast reinforced concrete buildings with dowel pin connections[J]. *Journal of Building Engineering*. 2016, 7: 224-238.
- [21] Kremmyda GD, Fahjan YM, Tsoukantas SG. Nonlinear FE analysis of precast RC pinned beam-to-column connections under monotonic and cyclic shear loading. *Bulletin of Earthquake Engineering* 2014;12(4):1615-1638.
- [22] Zoubek B, Isakovic T, Fahjan Y, Fischinger M. Cyclic failure analysis of the beam-to-column dowel connections in precast industrial buildings. *Engineering Structures* 2013;52:179-191.
- [23] Psycharis IN, Mouzakis HP. Shear resistance of pinned connections of precast members to monotonic and cyclic loading. *Engineering Structures* 2012;41:413-427.
- [24] Bahrami S, Madhkhan M, Shirmohammadi F, Nazemi N. Behavior of two new moment resisting precast beam to column connections subjected to lateral loading. *Engineering Structures* 2017;132:808-821.
- [25] Li SF, Li QL, Zhang H, Jiang HT, Yan L, Jiang WS. Experimental study of a fabricated confined

concrete beam-to-column connection with end-plates. *Construction and Building Materials* 2018;158:208-216.

- [26] Nzabonimpa JD, Hong WK, Kim J. Experimental and non-linear numerical investigation of the novel detachable mechanical joints with laminated plates for composite precast beam-column joint. *Composite Structures* 2018;185:286-303.
- [27] Nzabonimpa JD, Hong WK, Kim J. Nonlinear finite element model for the novel mechanical beam-column joints of precast concrete-based frames. *Computers & Structures* 2017;189:31-48.
- [28] Wang CL, Liu Y, Zheng XL, Wu J. Experimental investigation of a precast concrete connection with all-steel bamboo-shaped energy dissipaters. *Engineering Structures* 2019;178:298-308.
- [29] Wang HS, Marino EM, Pan P, Liu H, Nie X. Experimental study of a novel precast prestressed reinforced concrete beam-to-column joint. *Engineering Structures* 2018;156:68-81.
- [30] Priestley MJN, Tao JR. Seismic response of precast prestressed concrete frames with partially debonded tendons. *PCI Journal* 1993;38(1):58-69.
- [31] Morgen BG, Kurama YC. Seismic design of friction-damped precast concrete frame structures. *Journal of Structural Engineering* 2007;133(11):1501-1511.
- [32] Rodgers GW, Solberg KM, Mander JB, Chase JG, Bradley BA, Dhakal RP. High-force-to-volume seismic dissipaters embedded in a jointed precast concrete frame. *Journal of Structural Engineering* 2012;138(3):375-386.
- [33] Koshikawa T. Moment and energy dissipation capacities of post-tensioned precast concrete connections employing a friction device. *Engineering Structures* 2017;138:170-180.
- [34] Henin E, Morcou G. Non-proprietary bar splice sleeve for precast concrete construction. *Engineering Structures* 2015;83:154-162.
- [35] Englekirk RE. Overview of PCI workshop on effective use of precast concrete for seismic resistance. *PCI Journal* 1986;31(6):48-58.
- [36] Lu Z, Wang ZX, Li JB, Huang B. Studies on seismic performance of precast concrete columns with grouted splice sleeve. *Applied Sciences* 2017;7:571.
- [37] Ling JH, Abd Rahman AB, Ibrahim IS, Hamid ZA. Tensile capacity of grouted splice sleeves. *Engineering Structures* 2016;111:285-296.
- [38] Parks JE, Papulak T, Pantelides CP. Acoustic emission monitoring of grouted splice sleeve connectors and reinforced precast concrete bridge assemblies. *Construction and Building*

Materials 2016;122:537-547.

- [39] Ameli MJ, Brown DN, Parks JE, Pantelides CP. Seismic column-to-footing connections using grouted splice sleeves. *ACI Structural Journal* 2016;113(5):1021-1030.
- [40] Haber ZB, Saiidi MS, Sanders DH. Seismic performance of precast columns with mechanically spliced column-footing connections. *ACI Structural Journal* 2014;111(3):639-650.
- [41] Einea A, Yamane T, Tadros MK. Grout-filled pipe splices for precast concrete construction. *PCI Journal* 1995;40(1):82-93.
- [42] Lu ZW, Huang J, Dai SB, Liu JX, Zhang MZ. Experimental study on a precast beam-column joint with double grouted splice sleeves. *Engineering Structures* 2019;199:109589.
- [43] Cleland NM, Baber TT. Behavior of precast reinforced concrete ledger beams. *PCI journal* 1986;31(2):96-117.
- [44] Baghdadi A, Heristchian M, Ledderose L, Kloft H. Experimental and numerical assessment of new precast concrete connections under bending loads. *Engineering Structures* 2020;212:110456.
- [45] Yan QS, Sun BW, Liu XM, Wu J. The effect of assembling location on the performance of precast concrete beam under impact load. *Advances in Structural Engineering* 2017;21(8):1211-1222.
- [46] Le TD, Pham TM, Hao H, Hao YF. Flexural behaviour of precast segmental concrete beams internally prestressed with unbonded CFRP tendons under four-point loading. *Engineering Structures* 2018;168:371-383.
- [47] Lu ZW, Huang J, Li YB, Dai SB, Peng Z, Liu X, et al. Mechanical behaviour of grouted sleeve splice under uniaxial tensile loading. *Engineering Structures* 2019;186:421-435.
- [48] JG/T408-2013. Cementitious grout for coupler of rebar splicing. Beijing: Standards Press of China; 2013.
- [49] GB/T50152-2012. Standard for test method of concrete structures. Beijing: China Architecture and Building Press; 2012.
- [50] Cai XN, Pan ZF, Zhu YZ, Gong N, Wang YW. Experimental and numerical investigations of self-centering post-tensioned precast beam-to-column connections with steel top and seat angles. *Engineering Structures* 2021;226:111397.
- [51] Liu HT, Wang ZY, Du XL, Shen GQP. The seismic behaviour of precast concrete interior joints with different connection methods in assembled monolithic subway station. *Engineering Structures* 2021;232:111799.

- [52] Wang X, Li LZ, Deng BY, Zhang Z, Jia L. Experimental study on seismic behavior of prefabricated RC frame joints with T-shaped columns. *Engineering Structures* 2021;233:111912.
- [53] Sun ZY, Fu LC, Feng DC, Vatuloka AR, Wei Y, Wu G. Experimental study on the flexural behavior of concrete beams reinforced with bundled hybrid steel/FRP bars. *Engineering Structures* 2019;197:109443.
- [54] Ding T, Xiao JZ, Chen E, Khan A. Experimental study of the seismic performance of concrete beam-column frame joints with DfD connections. *Journal of Structural Engineering* 2020;146(4):04020036.
- [55] GB50010-2010. Code for design of concrete structures. Beijing: China Architecture and Building Press; 2010.
- [56] Li HW, Chen WS, Hao H. Dynamic response of precast concrete beam with wet connection subjected to impact loads. *Engineering Structures* 2019;191:247-263.

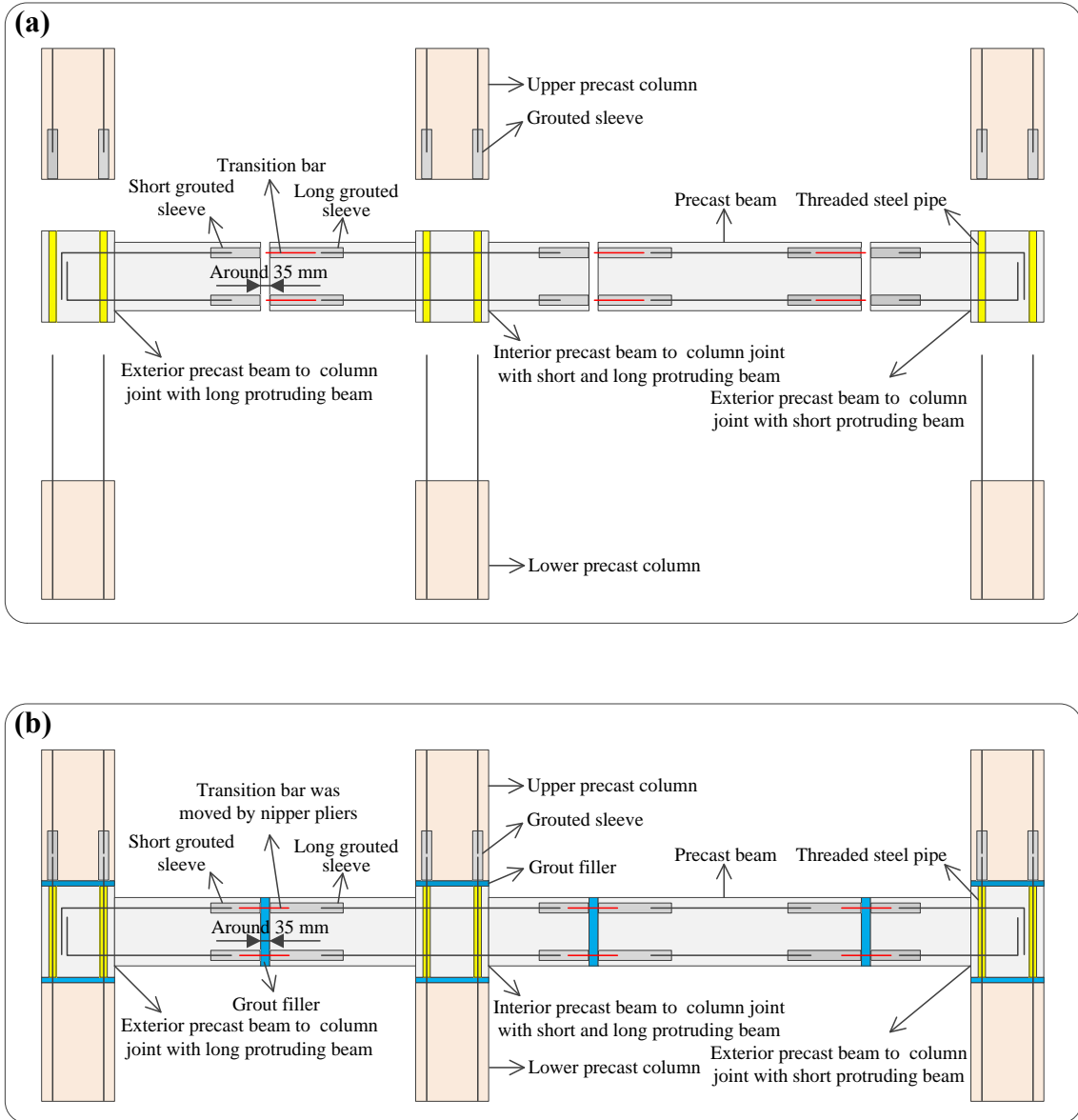


Fig. 1. Schematic diagram of the proposed precast concrete frame structure connected by double grouted sleeves: (a) before installation; (b) after installation.

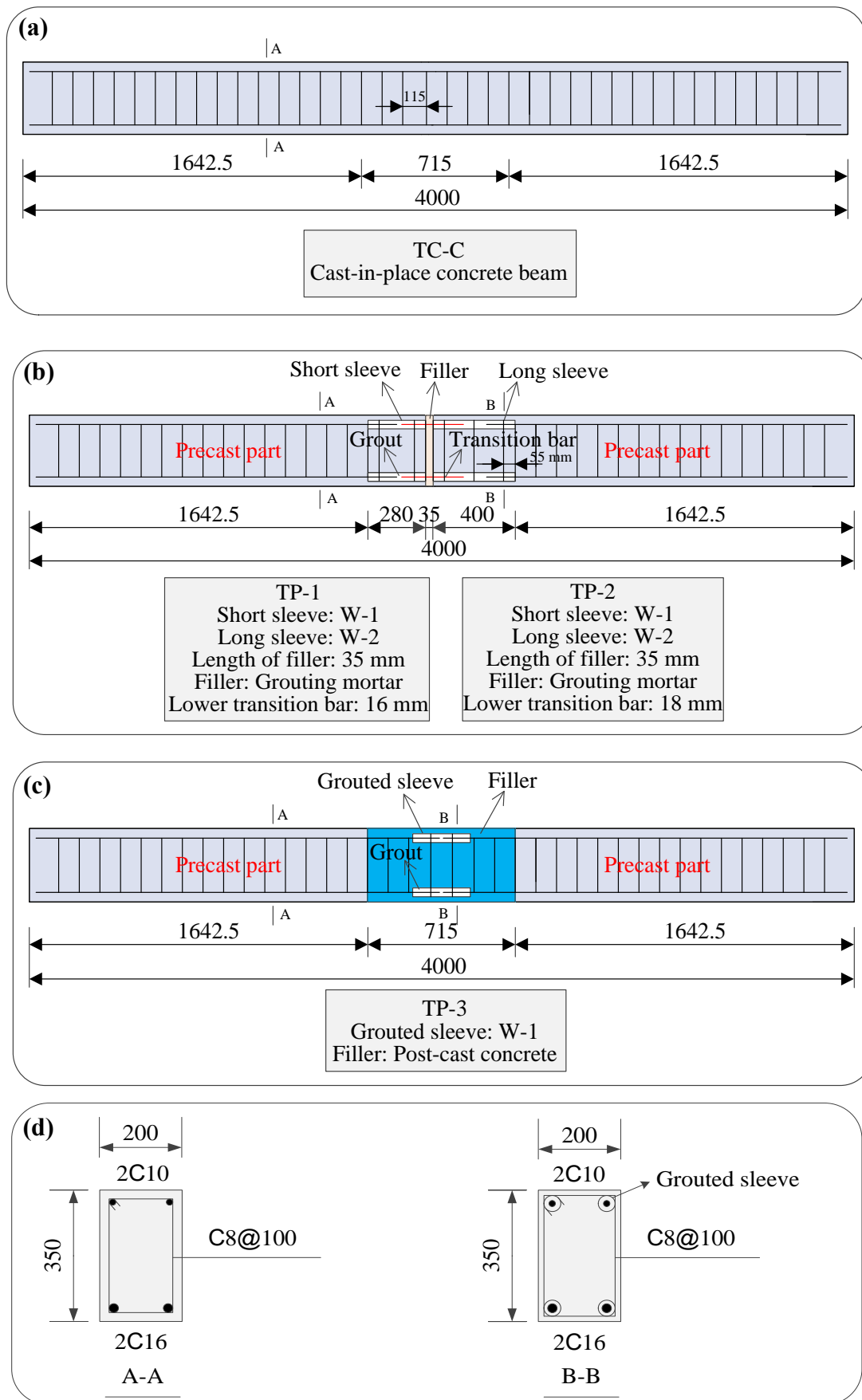
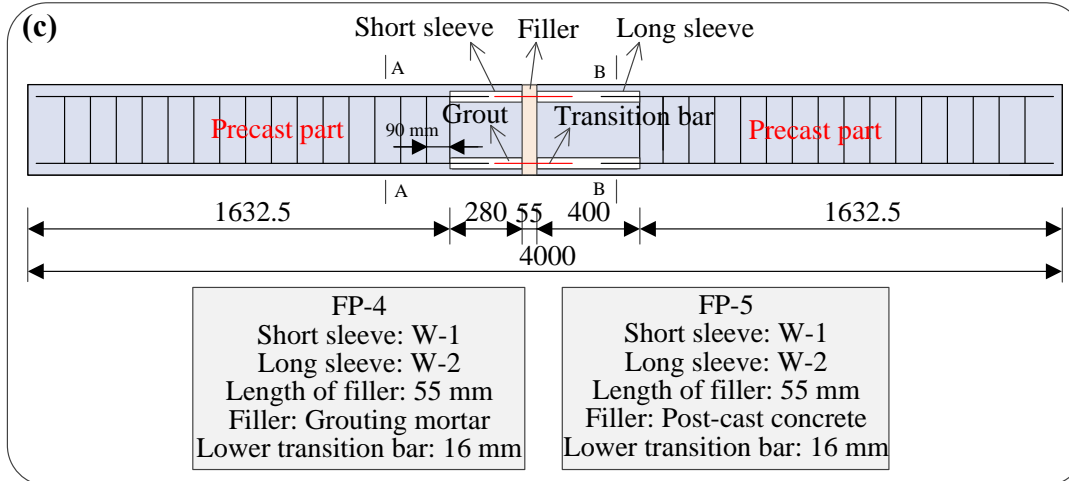
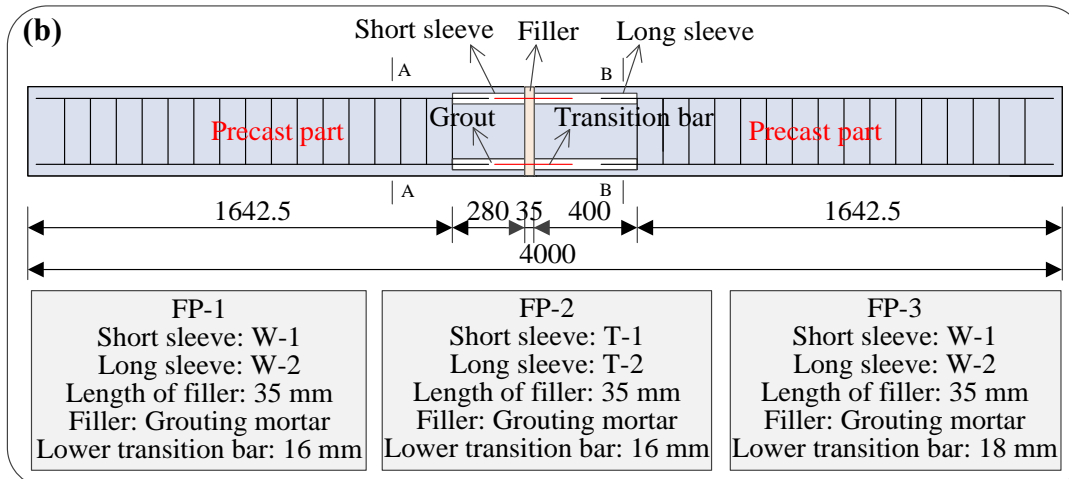
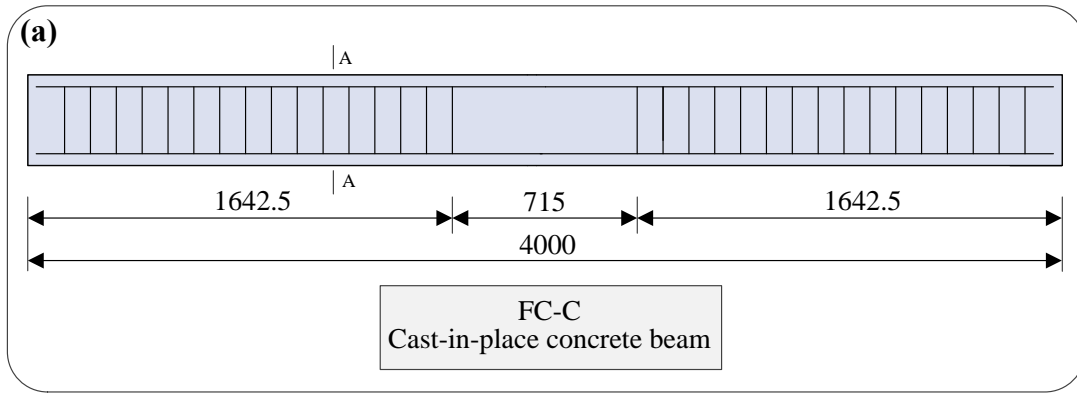


Fig. 2. Details of specimens for three-point bending tests (in mm): (a) TC-C; (b) TP-1 and TP-2; (c) TP-3; (d) cross section details.



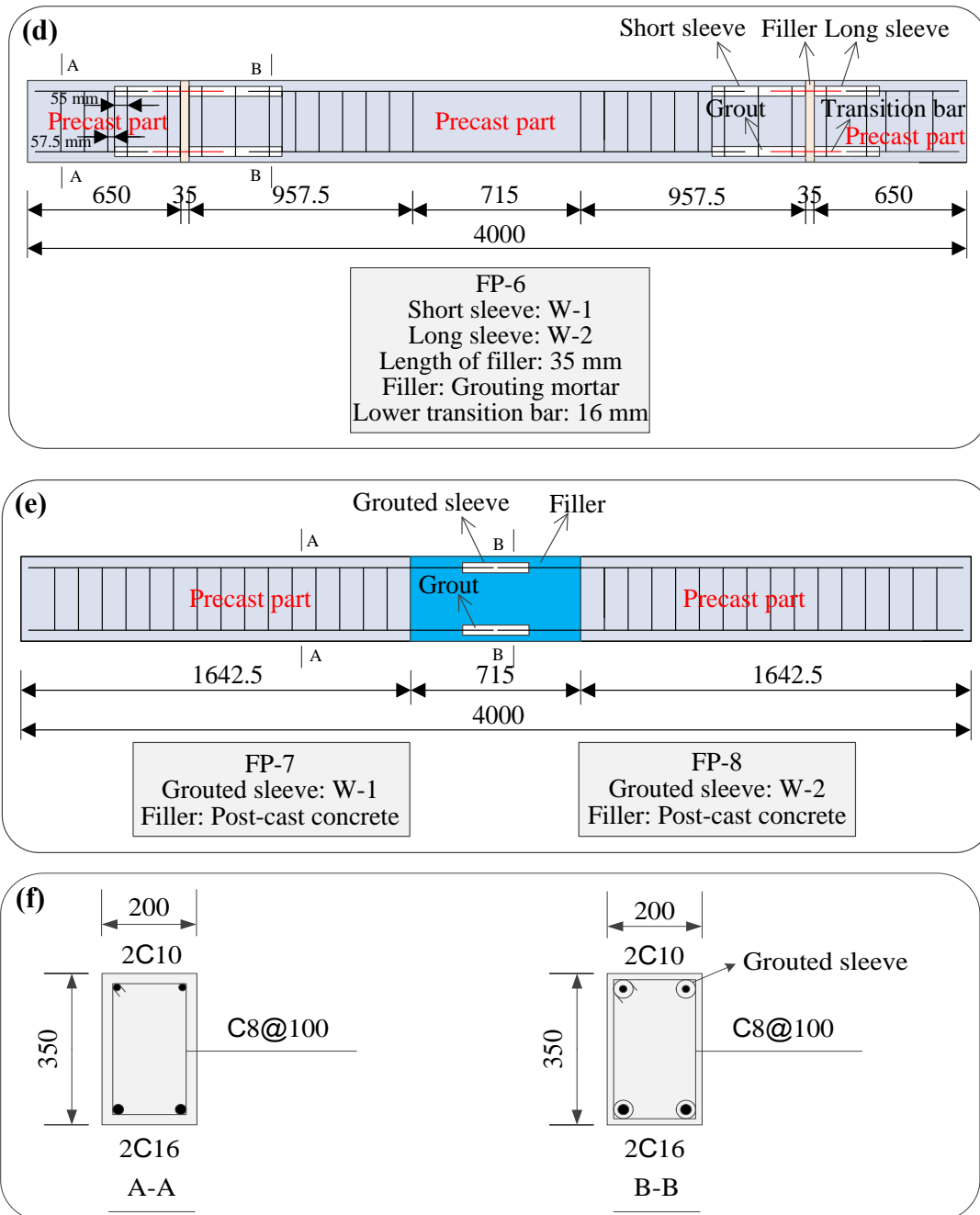


Fig. 3. Details of specimens for four-point bending tests (in mm): (a) FC-C; (b) FP-1, FP-2 and FP-3; (c) FP-4 and FP-5; (d) FP-6; (e) FP-7 and FP-8; (f) cross section details.

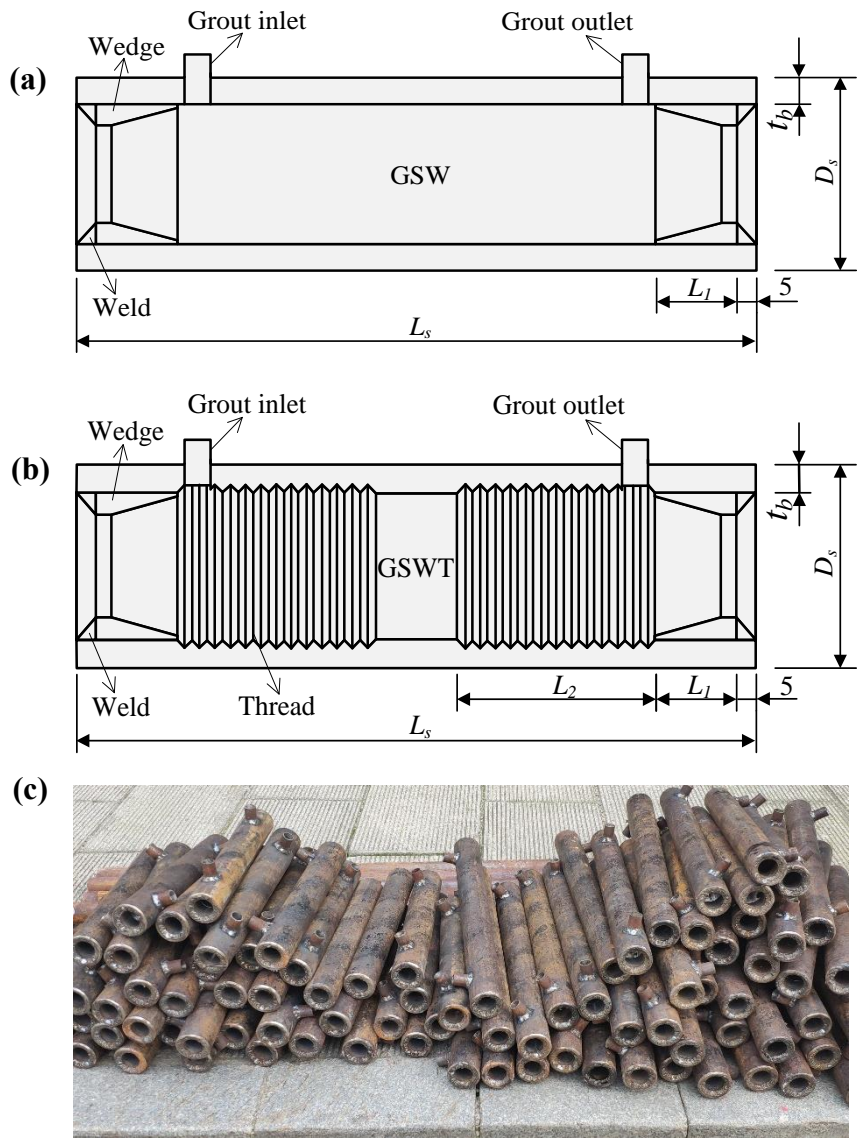


Fig. 4. Details of grouted sleeves: (a) GSW (W-1 and W-2); (b) GSWT (T-1 and T-2); (c) image.

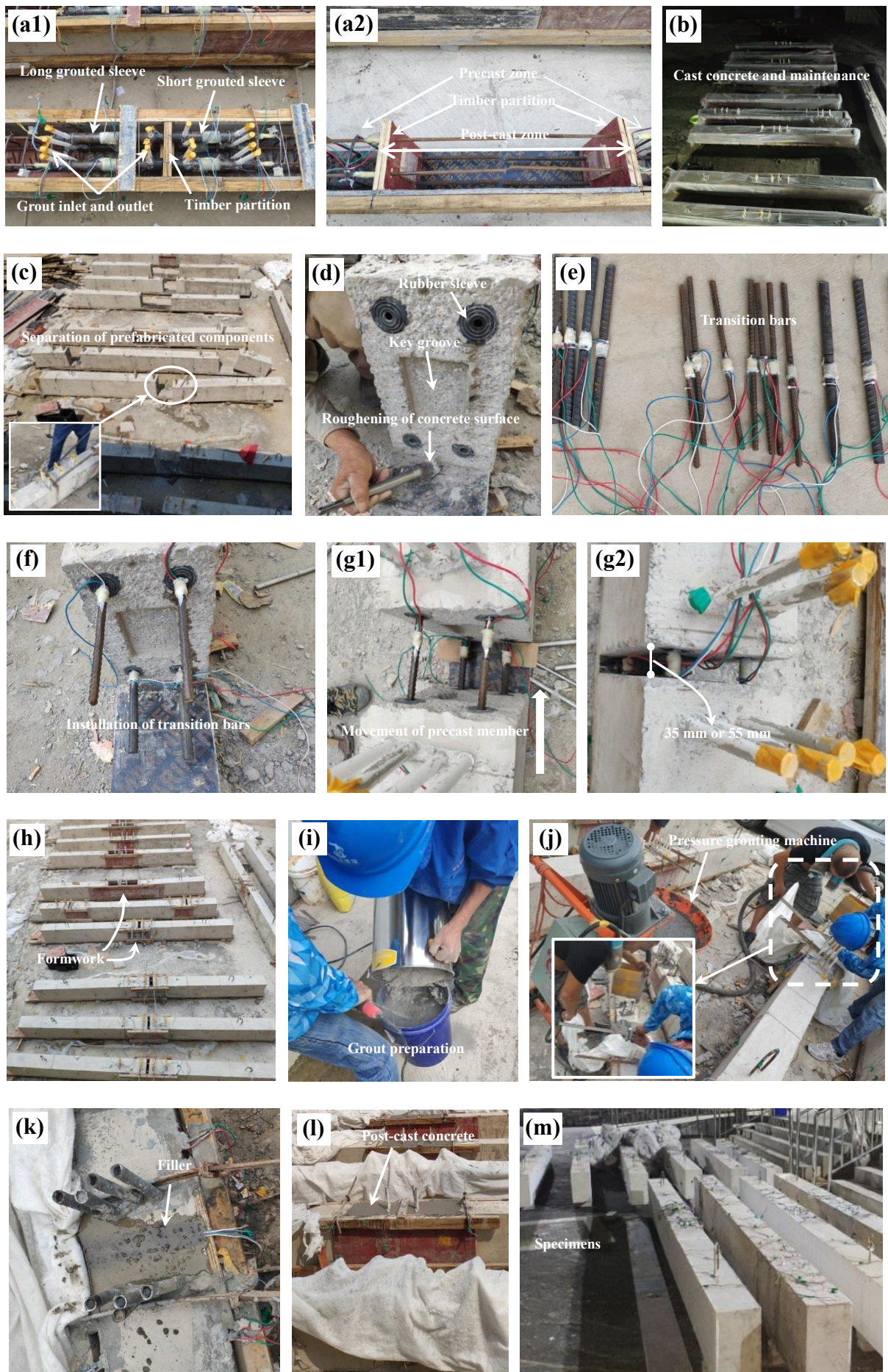


Fig. 5. Fabrication of precast specimens.

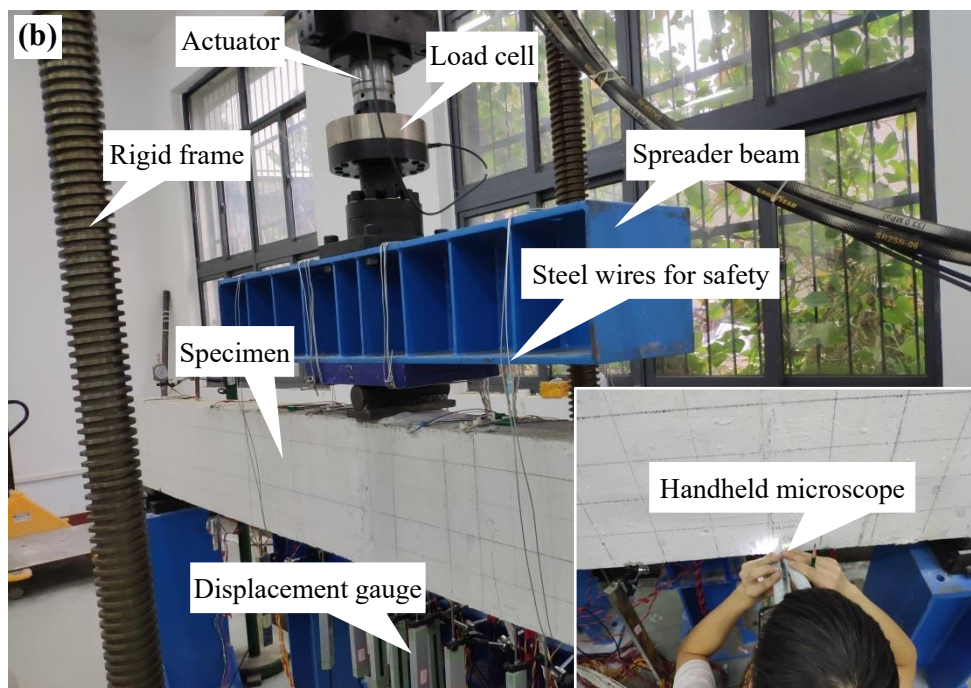
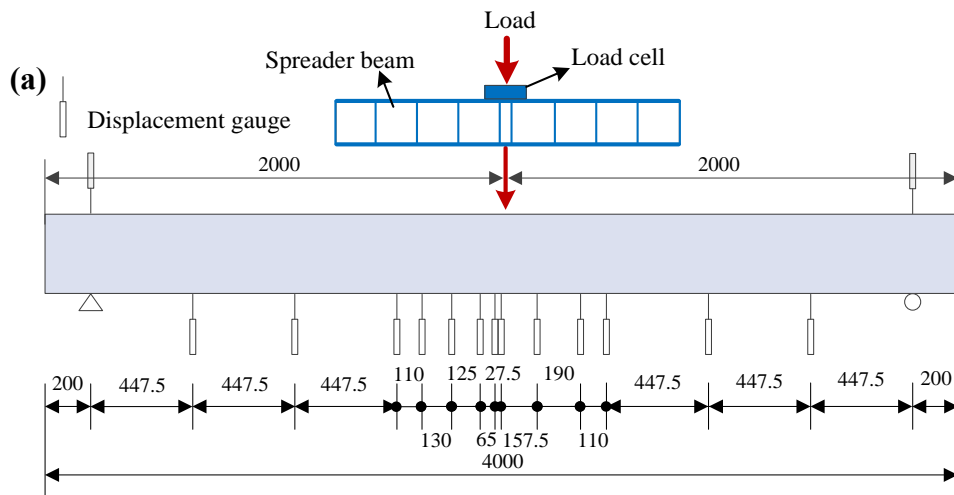
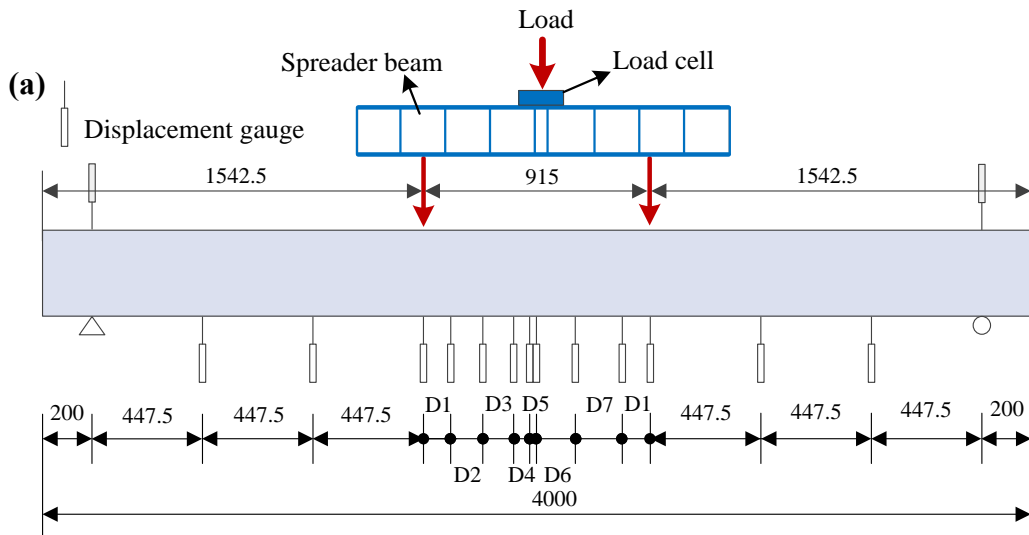


Fig. 6. Three-point bending test setup (in mm): (a) schematic diagram; (b) image.



For FP-4 and FP-5: D1=100; D2=130; D3=125; D4=85; D5=27.5; D6=157.5; D7=180.
 For FC-C, FP-1, FP-2, FP-3, FP-6, FP-7 and FP-8: D1=110; D2=130; D3=125; D4=65; D5=27.5;
 D6=157.5; D7=190.

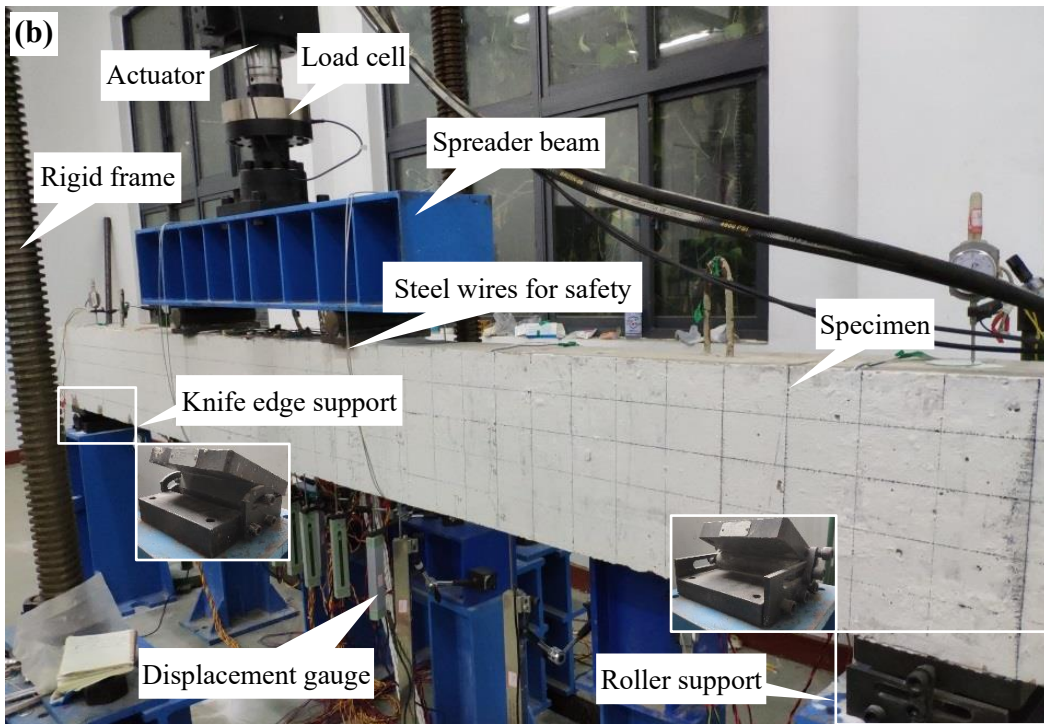


Fig. 7. Four-point bending test setup (in mm): (a) schematic diagram; (b) image.

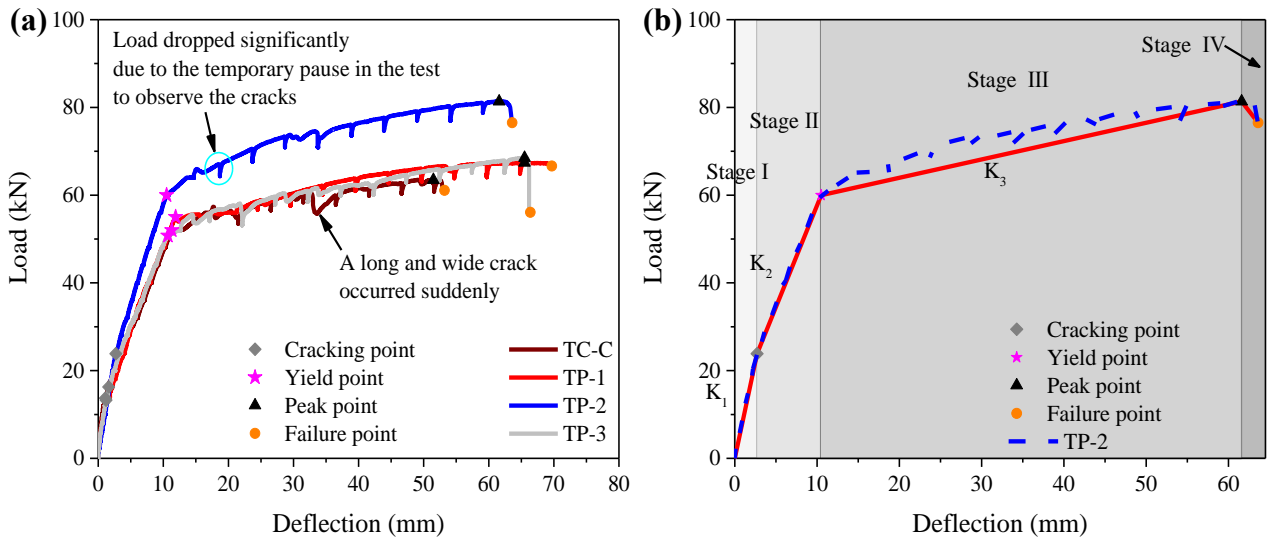


Fig. 8. Load-deflection response at midspan for all the specimens (a) and the specimen TP-2 (b) under three-point bending.

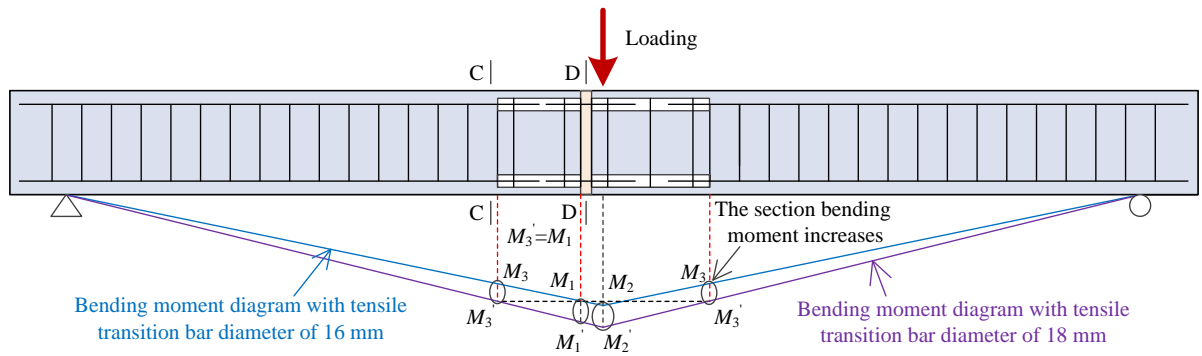


Fig. 9. Bending moment diagram for the beams TP-1 and TP-2.



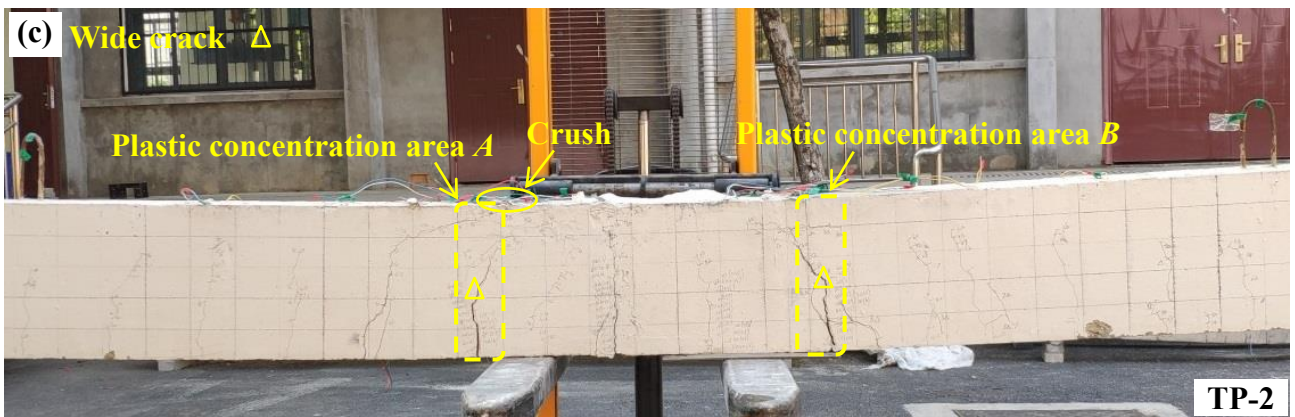


Fig. 10. Failure modes of specimens under three-point bending: (a) TC-C; (b) TP-1; (c) TP-2; (d) TP-3.

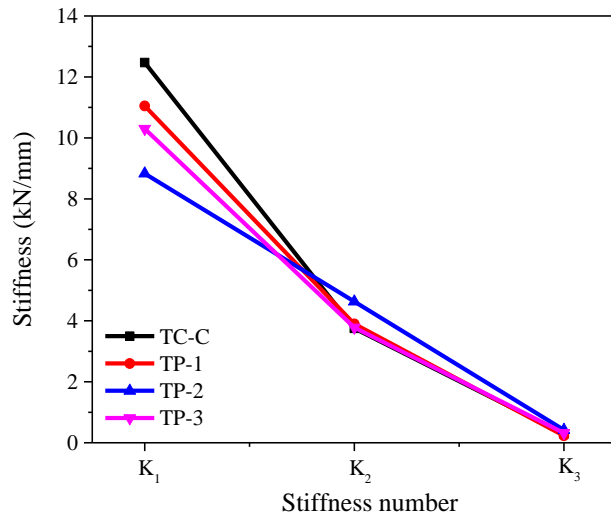
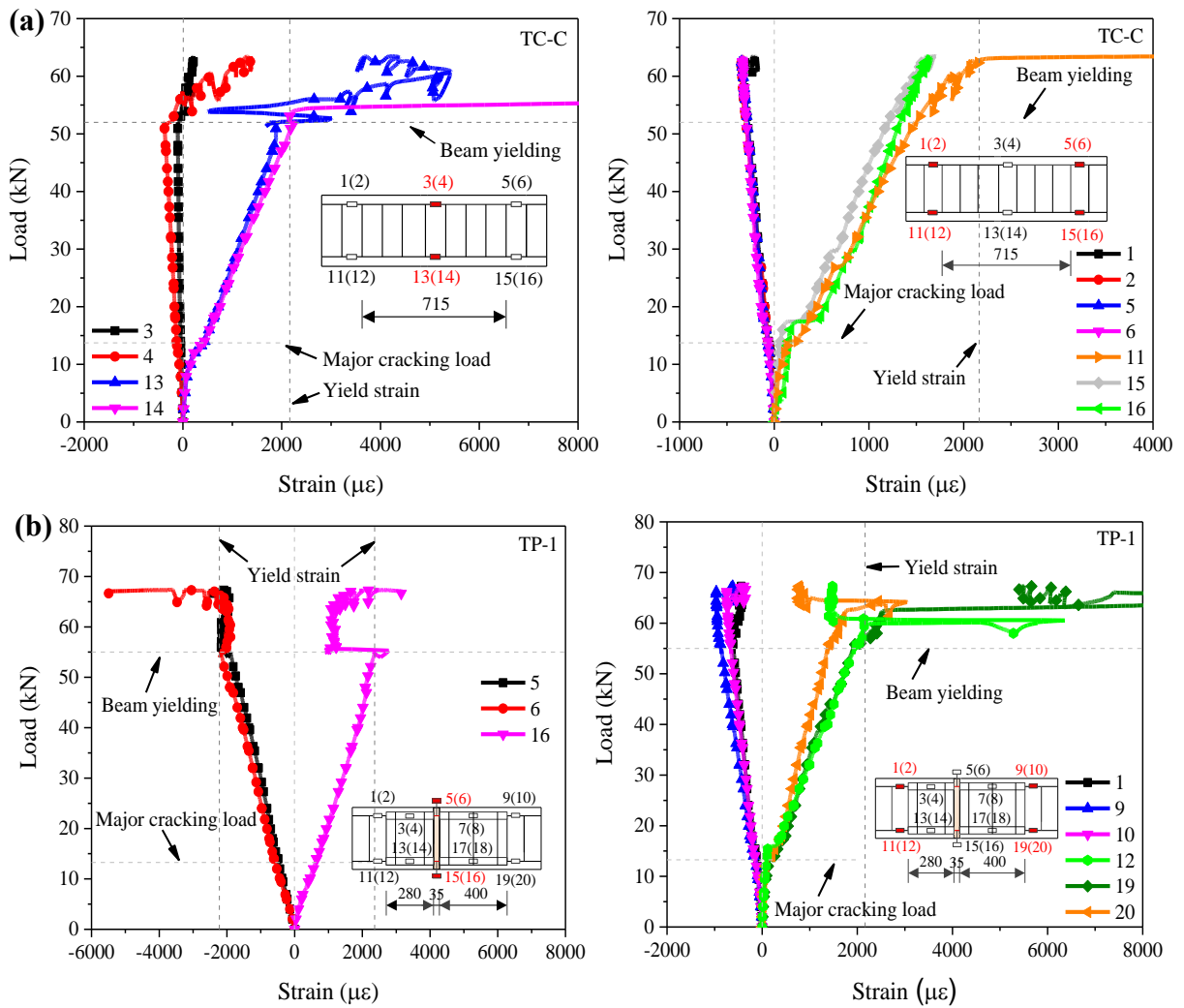


Fig. 11. Stiffness degradation of beams under three-point bending.



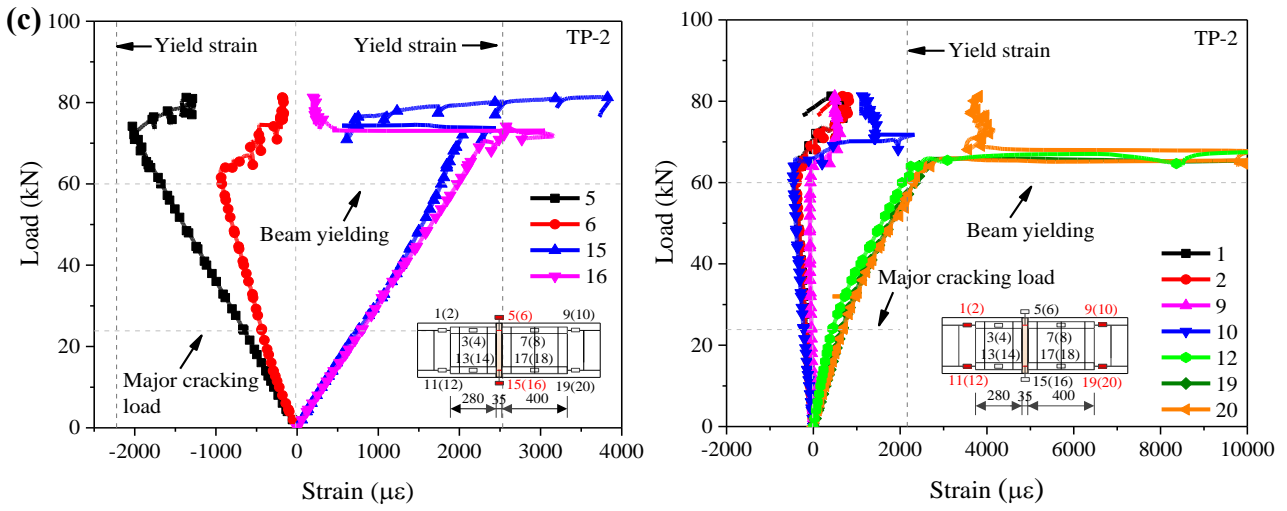


Fig. 12. Load-strain response of rebar in beams under three-point bending: (a) TC-C; (b) TP-1; (c) TP-2.

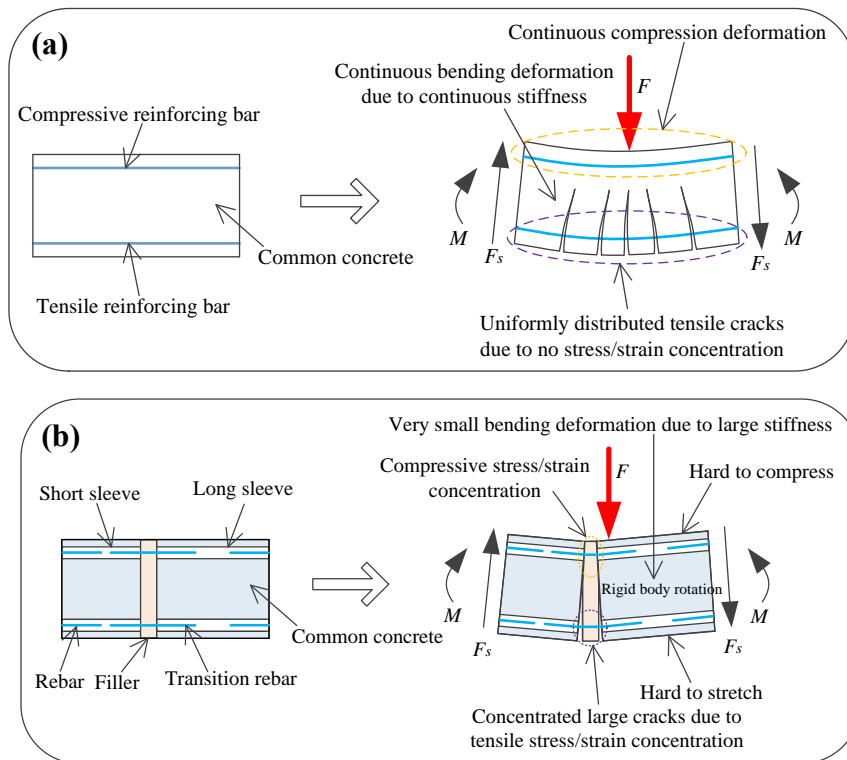


Fig. 13. Schematic diagram of bending deformation of the beams in the midspan area: (a) cast-in-place beam; (b) precast beam with double steel sleeves.

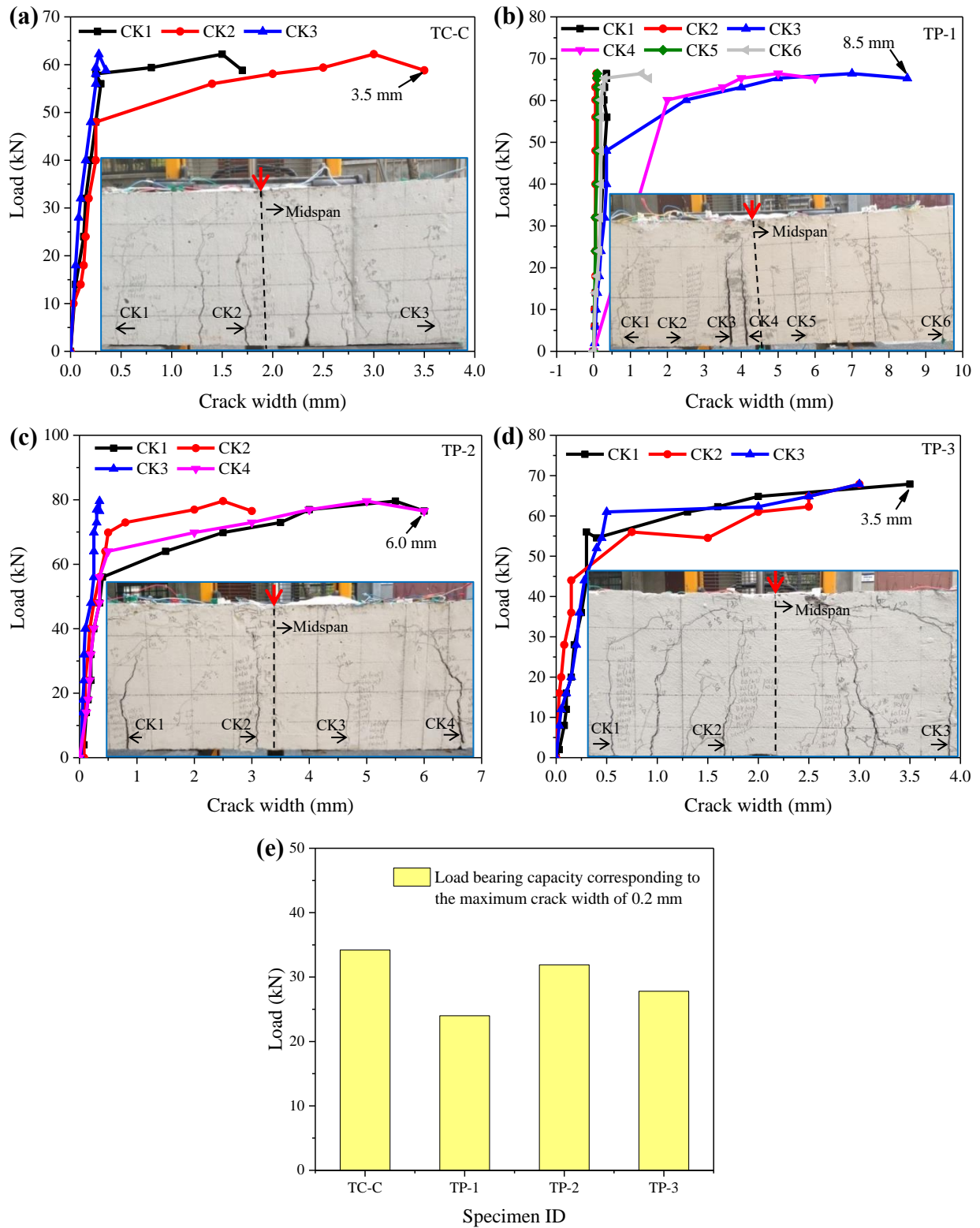


Fig. 14. Crack width of specimens under three-point bending: (a)-(d) load-crack width curves; (e) comparison of load bearing capacity corresponding to the maximum crack width of 0.2 mm.

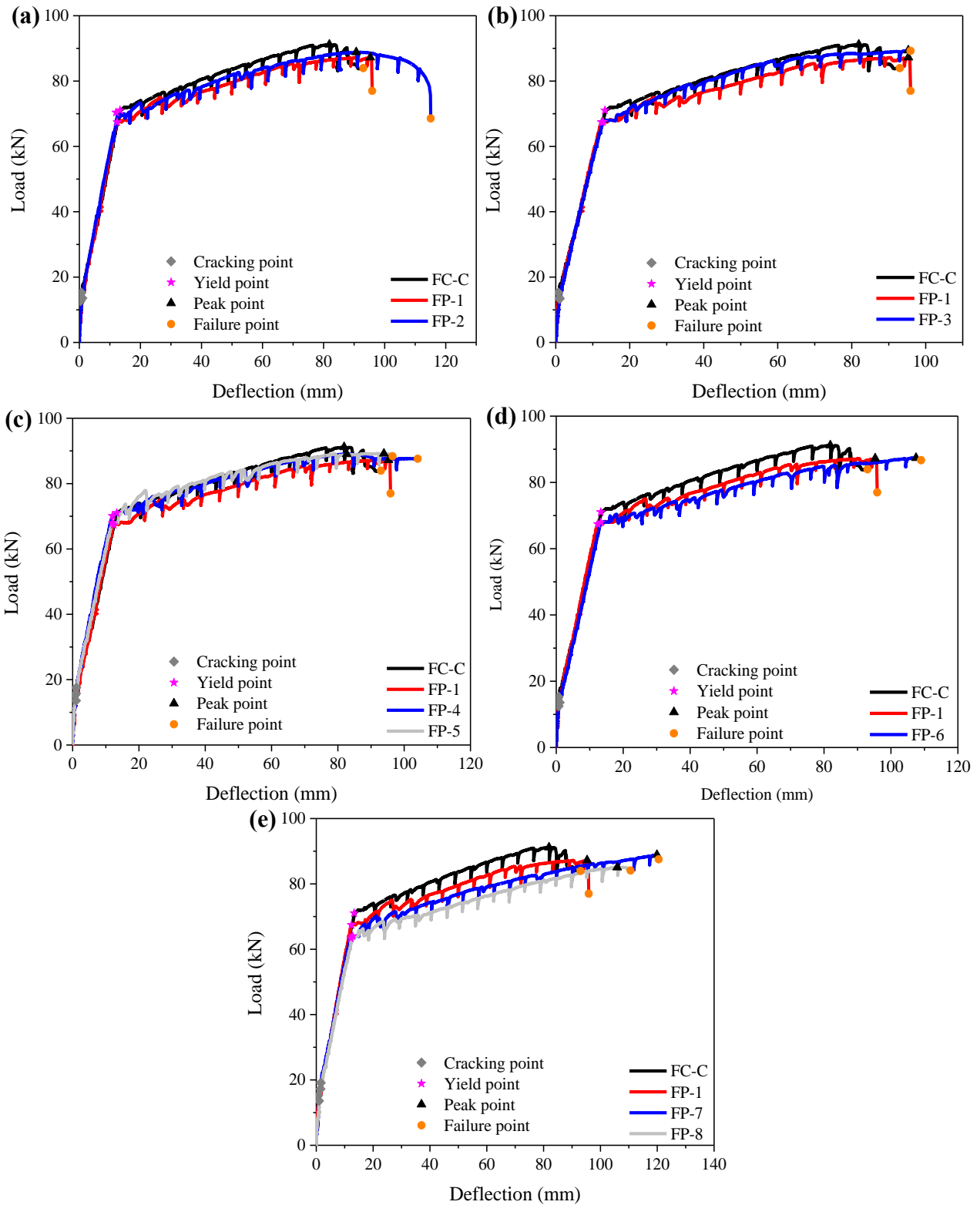
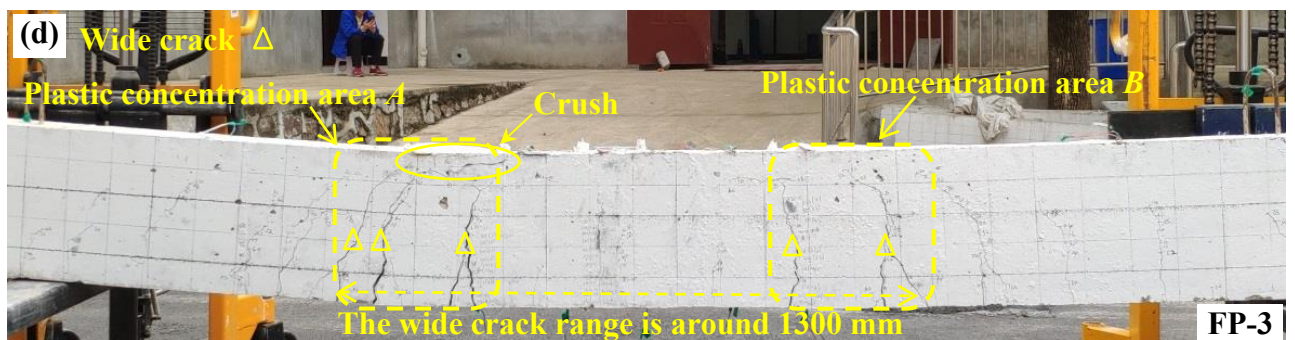
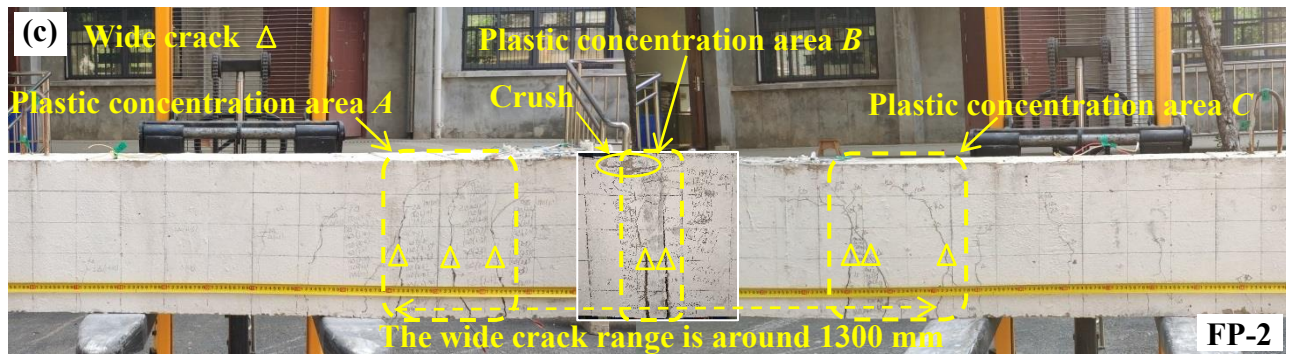
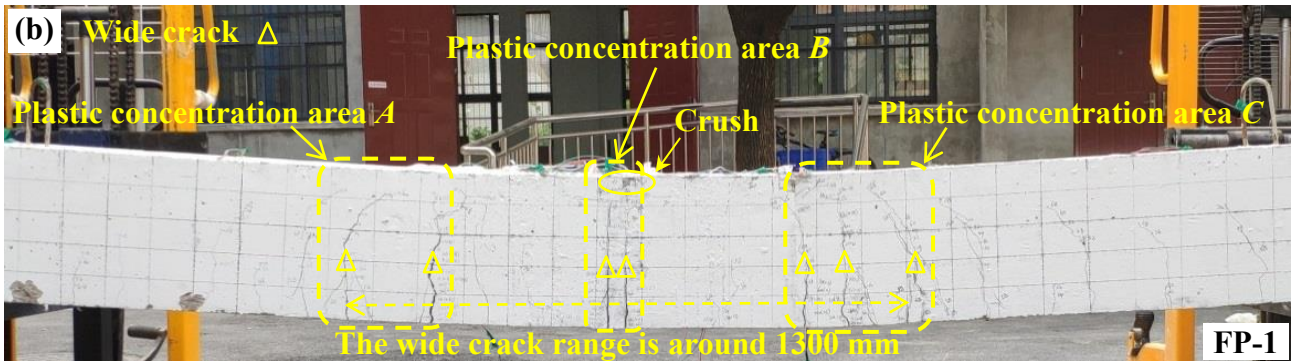
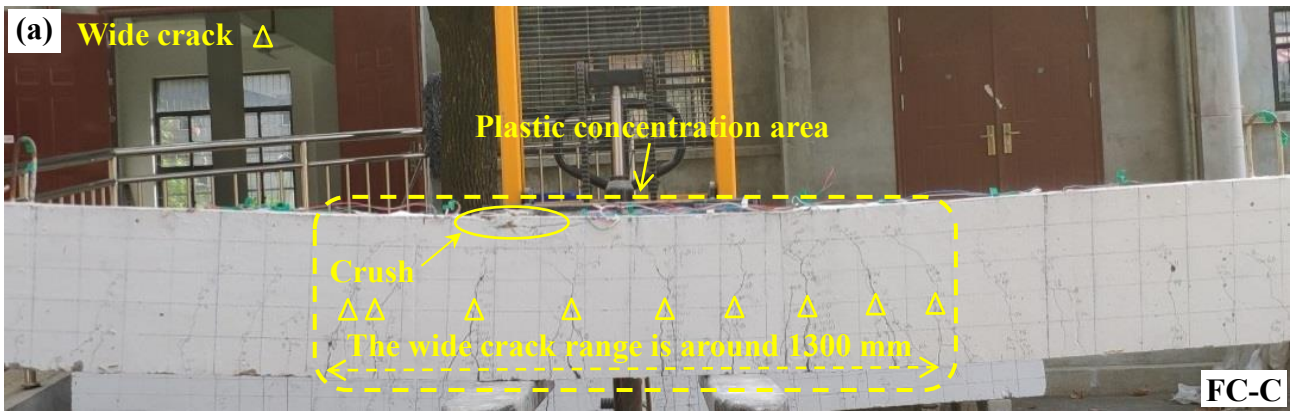


Fig. 15. Load-deflection response at midspan for specimens under four-point bending.



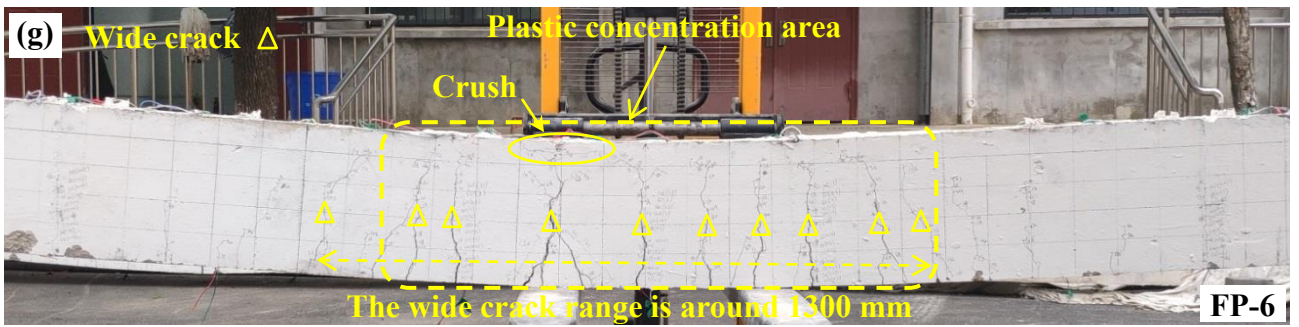


Fig. 16. Failure modes of specimens under four-point bending: (a) FC-C; (b) FP-1; (c) FP-2; (d) FP-

3; (e) FP-4; (f) FP-5; (g) FP-6; (h) FP-7; (i) FP-8.

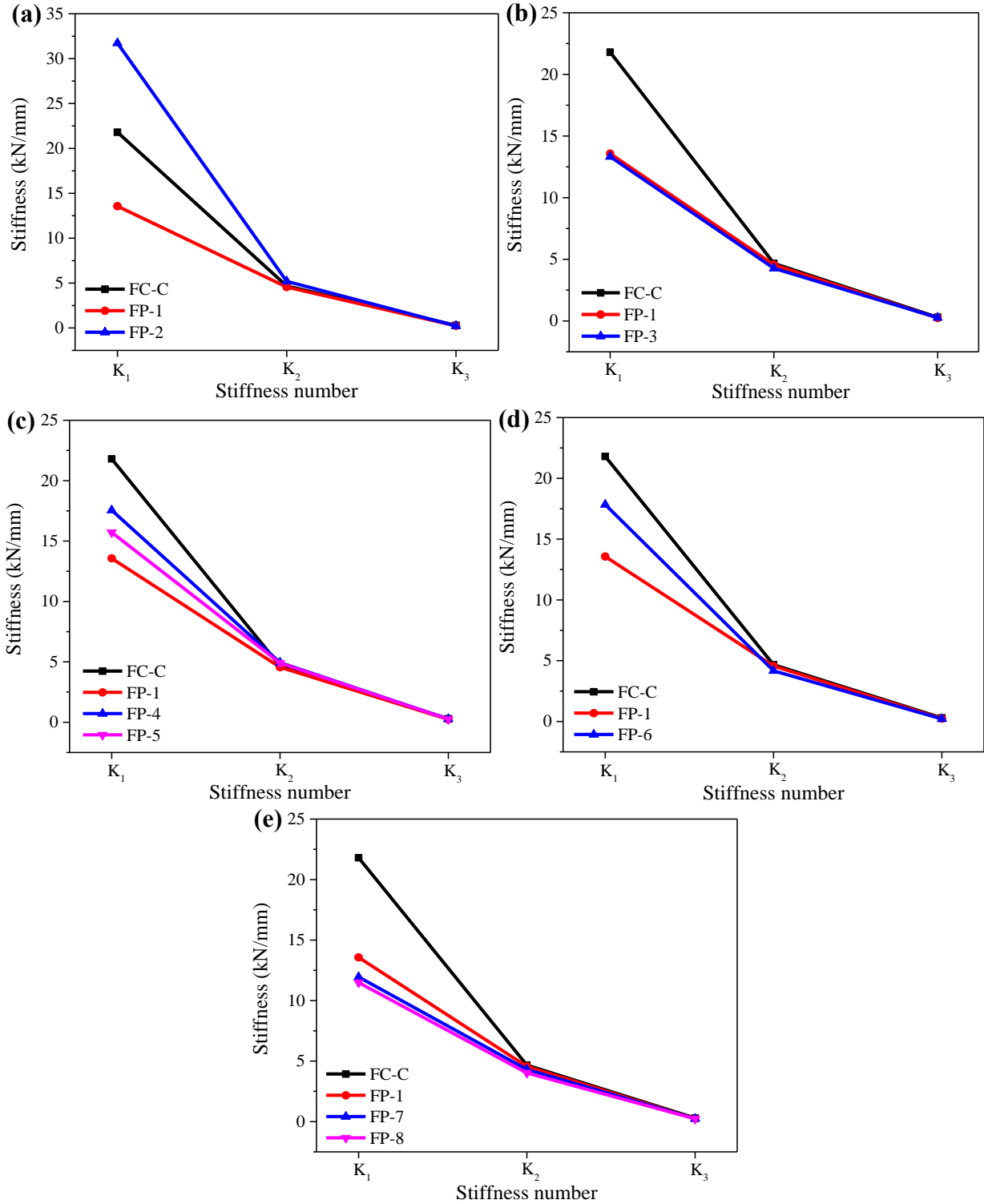
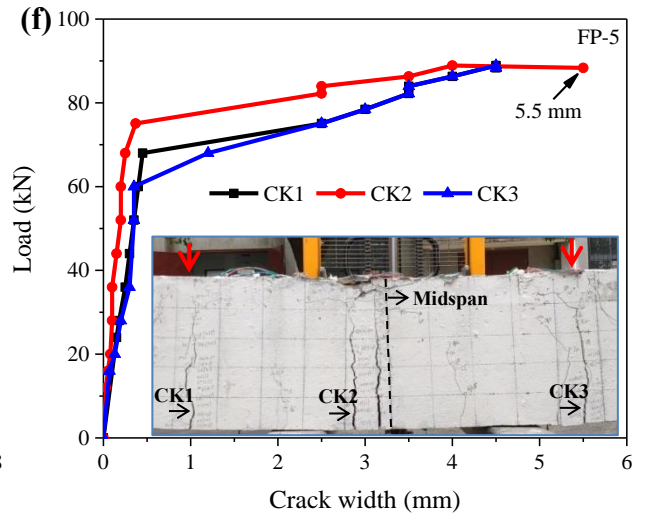
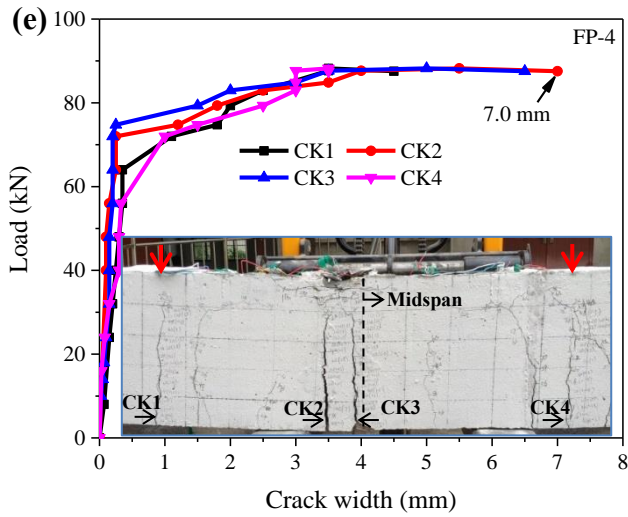
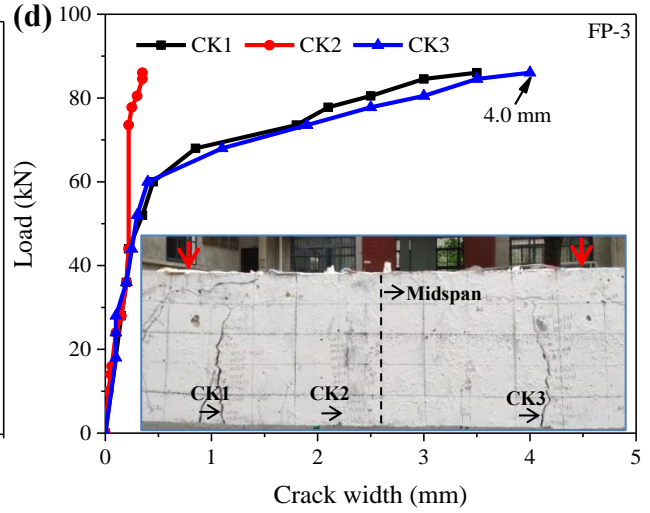
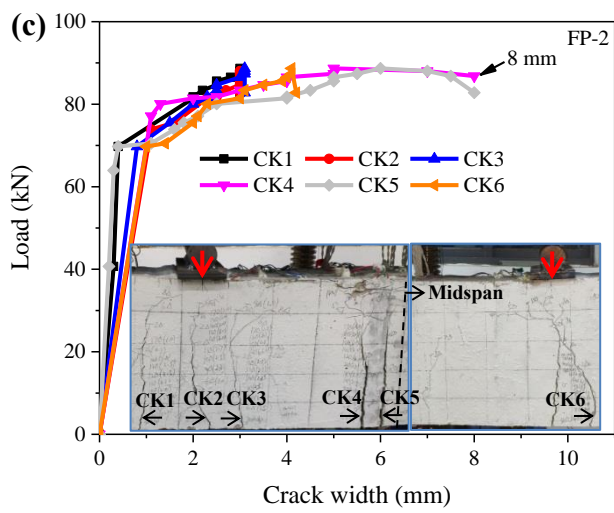
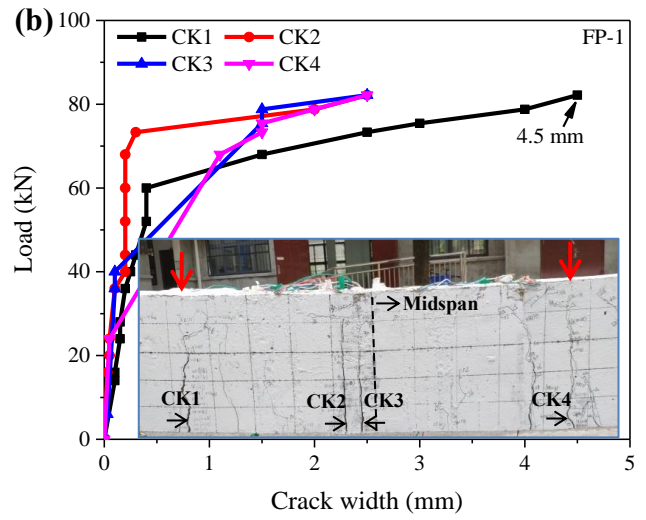
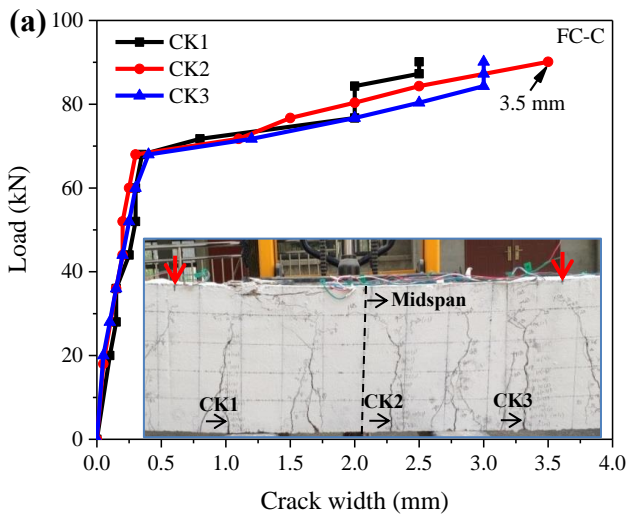


Fig. 17. Stiffness degradation of beams under four-point bending.



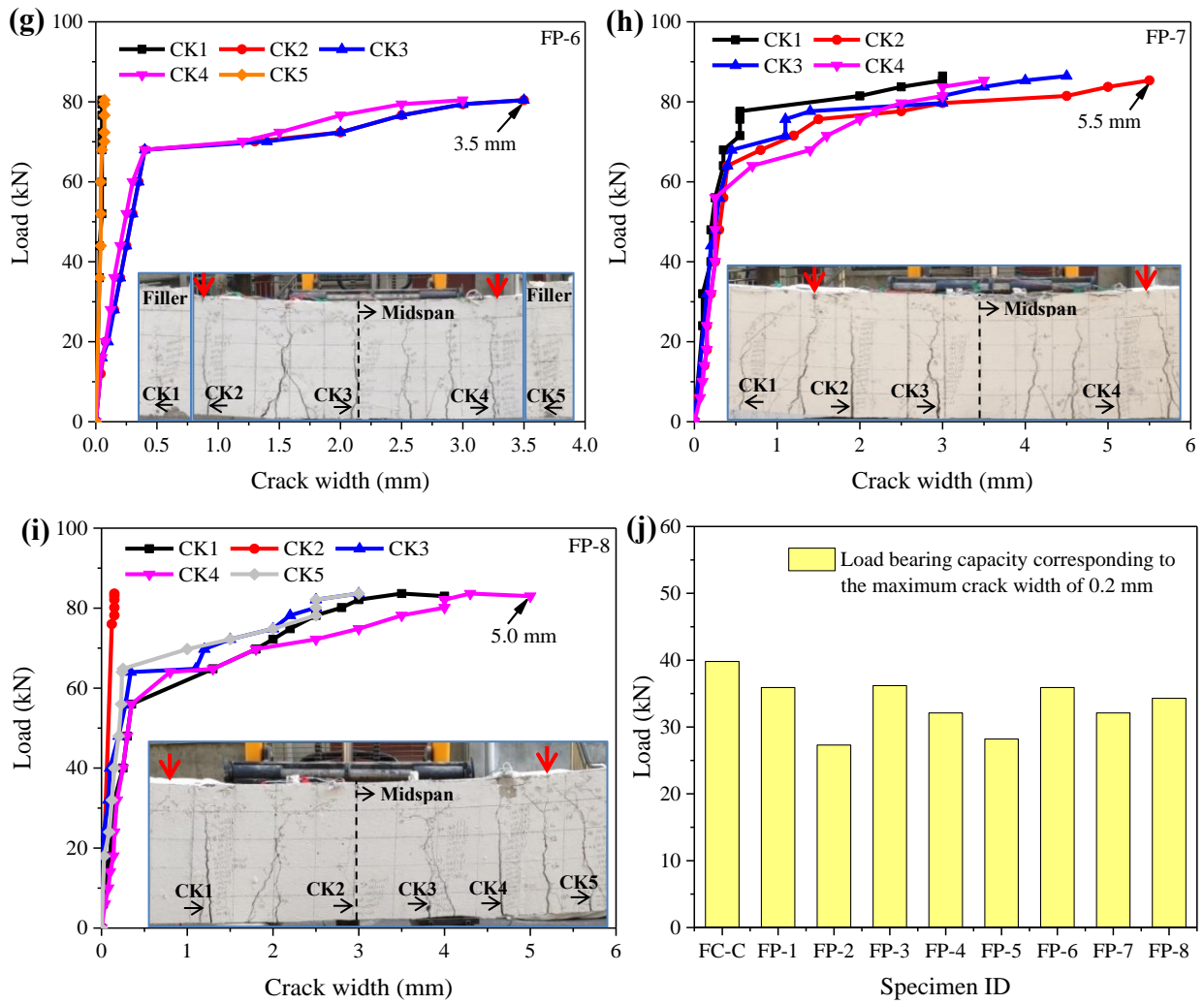


Fig. 18. Crack width of specimens under four-point bending: (a)-(i) load-crack width curves; (j) comparison of load bearing capacity corresponding to the maximum crack width of 0.2 mm.

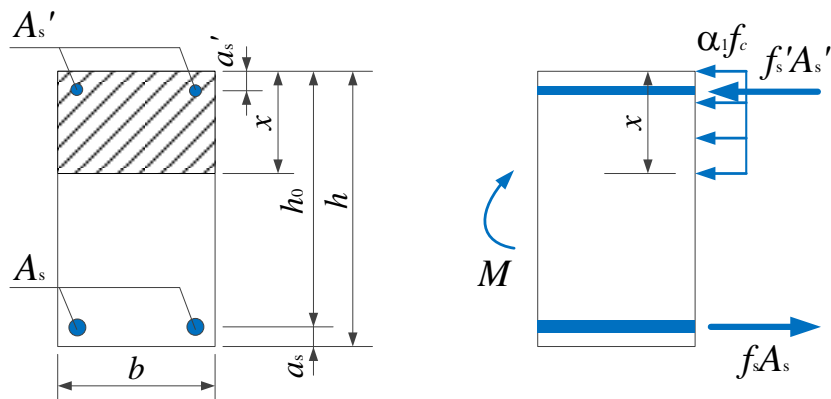


Fig. 19. Schematic diagram for calculating the flexural ability of the specimen.

Table 1 Details of grouted sleeves.

Name of sleeve	Type of sleeve	Type of length	L_1 (mm)	L_2 (mm)	L_s (mm)	D_s (mm)	t_b (mm)
W-1	GSW	Short		/	280		
W-2	GSW	Long	30	/	400	42	5
T-1	GSWT	Short		85	280		
T-2	GSWT	Long		85	400		

Note: L_1 is the wedge length, L_2 is the distribution length of thread, L_s is the length of the grouted sleeve, D_s is the outer diameter of the grouted sleeve, and t_b is the wall thickness of the grouted sleeve.

Table 2 Specimen design details.

Specimen	Size (mm)	Type of joint	Short sleeve	Long sleeve	Filler	L_g (mm)	d_b (mm)	N_g (mm)	Type of loading
TC-C		Monolithic	/	/	/	/	/	0	
TP-1	200 × 350	Double sleeves	W-1	W-2	Grouting mortar	35	16	1	Three-point bending
TP-2		Double sleeves	W-1	W-2	Grouting mortar	35	18	1	
TP-3		Single sleeve	W-1	/	Post-cast concrete	715	/	1	
FC-C		Monolithic	/	/	/	/	/	0	
FP-1		Double sleeves	W-1	W-2	Grouting mortar	35	16	1	
FP-2		Double sleeves	T-1	T-2	Grouting mortar	35	16	1	
FP-3		Double sleeves	W-1	W-2	Grouting mortar	35	18	1	
FP-4	200 × 350	Double sleeves	W-1	W-2	Grouting mortar	55	16	1	Four-point bending
FP-5		Double sleeves	W-1	W-2	Post-cast concrete	55	16	1	
FP-6		Double sleeves	W-1	W-2	Grouting mortar	35	16	2	
FP-7		Single sleeve	W-1	/	Post-cast concrete	715	/	1	
FP-8		Single sleeve	W-2	/	Post-cast concrete	715	/	1	

Note: L_g is the connecting length (i.e. gap length) of precast concrete components, d_b is the transition bar diameter, and N_g is the number of the gap.

Table 3 Material properties of concrete, post-cast concrete, grout and grouting mortar.

Sample	Compressive strength (MPa)	Flexural strength (MPa)
Concrete	31.2	/
Post-cast concrete	29.9	/
Grout	93.5	15.4
Grouting mortar	63.3	11.2

Table 4 Material properties of reinforcement.

Type of rebar	Grade	Diameter (mm)	f_y (MPa)	f_u (MPa)	E_b (GPa)
Stirrup		8	414	611	200
Longitudinal bar 1#		10	445	610	200
Longitudinal bar 2#	HRB400	16	433	611	200
Transition bar 1#		16	465	566	200
Transition bar 2#		18	507	621	200

Note: f_y is the yield strength of rebar, f_u is the tensile strength of rebar, and E_b is the nominal elastic modulus.

Table 5 Load and midspan deflection of beams.

Beam	Yielding		Peak		Failure		μ_Δ	Loading type
	F_Y (kN)	Δ_Y (mm)	F_P (kN)	Δ_P (mm)	F_F (kN)	Δ_F (mm)		
TC-C	52.00	11.3	63.48	51.5	61.09	53.2	4.71	Three-point
TP-1	55.01	11.9	67.40	65.5	66.64	69.7	5.86	
TP-2	60.00	10.5	81.35	61.6	76.50	63.6	6.06	
TP-3	50.76	10.7	68.52	65.5	56.09	66.4	6.21	
FC-C	71.06	13.3	91.17	81.9	83.95	93.0	7.00	Four-point
FP-1	67.44	12.4	87.25	95.3	77.00	95.9	7.73	
FP-2	70.39	12.0	88.84	90.7	68.55	115.1	9.59	
FP-3	67.50	12.8	89.38	95.3	89.26	95.9	7.49	
FP-4	70.12	12.0	89.02	82.7	87.60	104.1	8.68	
FP-5	68.00	12.0	89.20	93.9	88.41	96.5	8.04	
FP-6	67.92	13.3	87.39	107.5	86.70	109.0	8.20	
FP-7	63.35	12.2	88.87	119.9	87.52	120.5	9.88	
FP-8	64.01	12.8	85.07	105.9	84.11	110.6	8.64	

Note: F_Y , F_P , and F_F are the loads, Δ_Y , Δ_P and Δ_F are the corresponding displacements, and μ_Δ is the ductility ratio.

Table 6 Cracking parameters of beams.

Beam	Cracking- α		Cracking- β		Cracking point		Loading type
	F_α (kN)	Δ_α (mm)	F_β (kN)	Δ_β (mm)	F_T (kN)	Δ_T (mm)	
TC-C	/	/	6.0	0.3	13.72	1.1	Three-point
TP-1	2.0	0.1	3.5	0.2	13.26	1.2	
TP-2	/	/	/	/	23.85	2.7	
TP-3	2.0	0.1	16.0	1.7	16.28	1.6	
FC-C	/	/	16.0	0.9	15.26	0.7	Four-point
FP-1	6.0	0.2	14.0	1.1	13.57	1.0	
FP-2	8.0	0.4	14.0	0.6	12.69	0.4	
FP-3	8.0	0.5	14.0	1.2	13.33	1.0	
FP-4	10.0	0.5	16.0	0.9	17.55	1.1	
FP-5	9.0	0.4	16.0	1.1	15.72	1.0	
FP-6	33.0	5.4	12.0	0.7	12.49	0.7	
FP-7	/	/	/	/	19.12	1.6	
FP-8	2.0	0	18.0	1.6	17.23	1.5	

Note: Cracking- α represents the cracking occurring at the interface between precast concrete and filler, Cracking- β denotes the cracking occurring in concrete for the control specimen and in precast concrete for the precast specimens, Cracking point is the first turning point in the load-displacement curve at midspan, F_α , F_β and F_T are the loads, and Δ_α , Δ_β and Δ_T are the corresponding midspan displacements.

Table 7 Comparison of measured and calculated load-carrying capacity of beams under three-point bending and four-point bending.

Specimen	M_{pre} (kN·m)	l_Δ (m)	F_{pre} (kN)	F_{exp} (kN)	F_{pre}/F_{exp}	Mean	Standard deviation
TC-C	64.09	1.80	71.21	63.48	1.12		
TP-1	59.37	1.74	68.24	67.40	1.01		
TP-2	64.09	1.44	89.01	81.35	1.09		
TP-3	64.10	1.66	77.23	68.52	1.13		
FC-C	64.10	1.34	95.67	91.17	1.05		
FP-1	59.37	1.34	88.61	87.25	1.02		
FP-2	59.37	1.34	88.61	88.84	1.00	1.06	0.049
FP-3	64.10	1.34	95.67	89.38	1.07		
FP-4	59.37	1.34	88.61	89.02	1.00		
FP-5	59.37	1.34	88.61	89.20	0.99		
FP-6	64.10	1.34	95.67	87.39	1.09		
FP-7	64.10	1.34	95.67	88.87	1.08		
FP-8	64.10	1.34	95.67	85.07	1.12		